Infrared Spectroscopy of (Nb+In) Co-Doped Rutile

by

Susan M. M. Yee

A THESIS SUBMITTED IN PARTIAL FULFILLMENT OF
THE REQUIREMENTS FOR THE DEGREE OF

MASTER OF SCIENCE

in

The Faculty of Graduate Studies

Department of Physics

BROCK UNIVERSITY

May 11, 2017

Dedication

I dedicate this work to my parents and to my cats who kept me company.

Abstract

This work studied rutile TiO_2 in pure form and co-doped with In (e^- acceptor) and Nb (e^- donor) at 5% and 10% to explore the effect of co-doping on the infrared active (IR) modes and the complex dielectric response function between 50 and 8000 cm^{-1} (1.5 - 240 THz, 0.00620 - 0.993 eV). Ceramic pellets of pure, 5% and 10% co-doped TiO_2 were prepared using a standard technique. Infrared reflectance (IR) measurements were taken and these data are supplemented with data from the literature to extend the range of frequencies beyond infrared. The dielectric function was determined two ways: (i) by fits of the reflectance to the factorized model of the dielectric function and (ii) by Kramers-Kronig analysis.

Co-doping rutile appears to decrease the permittivity at frequencies just below the mode that softens. It is possible that this is due to an increase in porosity resulting from co-doping. It appears that the increase in permittivity recently observed elsewhere [1] is not caused by doping induced changes to the phonon modes.

The overall effect of co-doping is to make the sample less reflective. The spectrum is composed of three wide, high-reflectance bands. For all levels of co-doping the first band is a mode that softens. The amount of doping does not affect the frequency of the mode that softens. The second and third bands are hard modes.

Co-doping appears to introduce four new, impurity, phonon modes that increase in oscillator strength with increasing co-doping level. These modes are centered near $\omega \approx 136$, 447, 654 and 793 cm^{-1} which are close to four, previously observed, Raman active modes in rutile. It is possible that the co-doping process causes the Raman modes to develop a dipole moment and become weakly IR active.

Acknowledgements

Dr. David A. Crandles
Dr. Maureen Reedyk
Dr. Shyamal K. Bose
Dr. Jory Korobanik
Mr. Nick Momot
Ms. Michelle Przedborski
Brock Physics Department
Brock Electronics Shop

Contents

List of Tables

List of Figures

Chapter 1

Introduction

1.1 Permittivity

In non-conductors (also called dielectrics) electrons cannot travel through the material freely. As a result bulk dielectric materials exposed to an external electric field $\vec{E}$ will form an internal electric field, the displacement field $\vec{D}$, inside the dielectric material. Linear dielectric materials are those in which the relationship between these two fields is linear; i.e. $\vec{D} = \varepsilon\vec{E}$, where $\varepsilon = \varepsilon_1 + i\varepsilon_2$ is the permittivity. The relative permittivity (or dielectric function) ε_r of a dielectric is the ratio of the permittivity ε to the permittivity of free space ε_0. In general, the permittivity is a complex tensor of rank two. Consequently, in anistropic materials, $\vec{D}$ is not parallel to $\vec{E}$. For many common materials ε is a complex scalar and this real part is usually less than roughly 10^2 in the low frequency ($0 - 10^6$Hz) range. The permittivity refers to the real part of the dielectric function. Permittivity of some common materials like water is about 80 and many industrial materials have ε_1 less than 100 [2, 3]. Some materials exhibit relative permittivity higher than 10^3, these materials are said to exhibit colossal permittivity (CP) or colossal dielectric constant (CDC). Table 1.1.1 shows the dielectric constants of some CDC materials.

Material	ε_1	Reference
$CaCu_3Ti_4O_{12}$	$\approx 10^5$	[4]
$Li_{0.01}Si_xNi_{0.99-x}O$	$\approx 5 \cdot 10^3$ at 1 kHz	[5]
$Ba_{0.95}La_{0.05}TiO_{3-x}$	$\approx 10^6$ at 1 kHz	[6]
$La_{15/8}Sr_{1/8}NiO_4$	$\approx 10^4$ at 1 GHz	[7]
$LuFe_2O_4$	$\approx 3 \cdot 10^4$ at 1 kHz	[8]

Table 1.1.1: Dielectric Constant of Some Materials with Colossal Dielectric Constants at room temperature.

Consider a capacitor where the plates are separated with vacuum or air. Replacing the vacuum with a dielectric will increase the capacitance by a factor ε_r (see [9] Example 4.6). Therefore dielectric materials can be used to increase the energy stored in a capacitor by a factor of ε_r over a "vacuum-filled" capacitor.

1.2 Previous Work on Colossal Permittivity

High dielectric constant materials allow the manufacture of smaller capacitors which results in higher circuit-density or smaller chips [10], or the manufacture of capacitors that can hold more energy. The development of microelectronic devices is driven by a great demand for smaller and faster devices and systems [6, 10]. Many important electronic circuits are made with capacitors such as high-energy-density storage devices e.g. static and dynamic, random access memory (RAM) [10, 11], radio frequency circuits in which up to 95% of the area of the chip is made of capacitors [10], and thin-film devices for wireless communication systems [11]. Modern electrical systems also need high energy-density storage devices such as found in cordless power tools and hybrid electric vehicles; a need supercapacitors can fill [12]. Solid CP materials may lead to better supercapacitors not only by increasing their energy density but also by improving their safety as current supercapacitors use liquid dielectric material [1]. It is not necessary to develop a pure compound for CP. Doping a parent material is a well established method to make colossal permittivity materials [1, 13–20]. It is not surprising that colossal permittivity has been widely studied for both theoretical and industrial reasons in many materials [1, 5–8, 10, 14–17, 19, 21–29].

CP was discovered in $CaCu_3Ti_4O_{12}$ (CCTO) around the year 2000 [4] and has been studied extensively by other groups [17, 27, 29–40]. Many CP materials have been discovered that exhibit the $CaCu_3Ti_4O_{12}$ perovskite-like crystal structure such as $Bi_{2/3}Cu_3Ti_4O_{12}$ [4, 41] and rare-earth element-based materials $Ln_{2/3}Cu_3Ti_4O_{12}$ where Ln = La, Ce, Pr, Nd, Sm, Eu, Gd, Tb, Dy, Ho, Er, Tm (a trivalent rare earth element) [4, 39]. Perovskites themselves have been the object of study for many years [42–49]. Other materials studied for CP properties include $BaTiO_3$ perovskites [50] in both doped[51] and undoped [23, 24] forms, $BaTiO_{3-x}$ [6, 23], $Ba_{0.95}La_{0.05}TiO_{3-x}$ ceramics [6], other barium-based ceramics [23–25, 52], $SrTiO_3$ [53, 54], $La_{15/8}Sr_{1/8}NiO_4$ [7], doped-NiO, $La_{15/8}Sr_{1/8}NiO_4$, $Ba(Fe_{0.5}Nb_{0.5})O_3$, $K_{0.3}MoO_3$ [16], Bi-substituted $LaMnO_3$ ceramics [55], $Li_{0.01}Si_xNi_{0.99-x}O$ ceramics [5], $Sr_{1-x}Pr_xTiO_3$ ceramics [54], $LuFe_2O_4$ [8], Y-doped $CaCu_3Ti_{4-x}Y_xO_{12-x/2}$ $(x = 0 - 0.1)$ [38] , composite $Ba(Zr_{0.2}Ti_{0.8})O_3$/carbon nanotube [52], and the surprisingly simple compound CuO (copper (II) oxide) [56].

TiO_2 has been a fruitful parent material for studying and making CP materials. The rutile phase (the most common and the most thermodynamically stable) has a perovskite-like structure where oxygen octahedra contain the Ti atom. Studies over decades have been made on undoped TiO_2 [57–63] and single-element doped TiO_2 including Nb [17, 59, 61, 64–71], Cr [72], Eu [73], and Fe [63, 74]. In 2013 Hu et al. [1] reported TiO_2

co-doped with different percentages of In and Nb showed CP which, importantly, shows low dielectric loss that is mostly temperature and frequency independent. More about this work will be presented in section 1.3.

1.3 Overview of Theoretical Explanations of Colossal Permitivitty

The complex dielectric function $\varepsilon^*(\omega)$ is the result of different phenomena: (1) fluctuations of molecular dipoles, (2) the migration of charge carriers (electrons, holes or ions), and/or (3) the separation of charges at boundary surfaces or interfaces which in turn leads to additional polarization. This last phenomenon can take place at inner dielectric boundary layers and/or at the contact surface between external electrodes and the sample. In practical terms samples (or commercial devices) must be connected to the measuring device to measure CP; hence, the observed CP of the entire circuit may be due to electrical effects from within the ceramic itself (intrinsic factors) as well as effects at the electrode-ceramic interface (extrinsic factors).

Ferroelectricity

Ferroelectric materials can exhibit a macroscopic dipole moment even when an external electric field is zero [75, 76]. Such a material can have a large permittivity near the ferroelectric-to-paraelectric phase transition temperature [76–78]. The perovskites ABO_3 where A = Ba, K, Pb, Li, La and B = Ti, Nb, Ta, Mn are examples of ferroelectric crystals [55, 76]. For example, Mamin et al. [28] studied CP in manganites. As an example of the complexity of CP behavior, where CP may be caused by more than one mechanism, Shen et al. [11] studied the Maxwell-Wagner effect in ferroelectric multilayered thin films. Conversely in nonferroelectric materials Lunkenheimer et al. [77] saw "that the largest intrinsic dielectric constant observed so far ... is of order 10^2."

The crystal structure is an important factor in the ferroelectric behavior of a crystal. For instance, the body center cubic (bcc) structure "prohibits ferroelectricity on symmetry grounds" [30]. Liu et al. [32] propose that CCTO shows "frustrated relaxor ferroelectric behavior" and with the displacement of Ti ions in the lattice this leads to the intrinsic high permittivity of CCTO. However, the transistion to the ferroelectric state is frustrated by the tilt of the TiO_6 octahedra in the CCTO lattice [4, 30, 32] and it appears that CP in CCTO is not the result of ferroelectric effects [34, 79].

Charge-Density Waves

A charge density wave (CDW) is a standing wave of charge density[80] that occurs in space in one dimensional, long molecular chains [81] or two dimensional objects such as thin epitaxial films [78] (see [82] for a classification of CDWs). The CDW interacts with the lattice atoms and is accompanied by periodic distortions in the atomic positions (for a simple text and visual description see [83]). However, the electronic CDW's period need not match the atomic lattice's periodic electric potential [78]. CDW systems can exhibit extremely high intrinsic dielectric constants of magnitudes up to 10^8 [77]. Unfortunately, CDW systems have a high dielectric loss and this limits their practical application in capacitor-based devices [78] . Lunkenheimer et al. [77] believe intrinsic CP behavior appears "only in CDW systems"; however, hopping charge transport, an intrinsic behavior, is also a candidate mechanism for CP.

Hopping Charge Transport

Hopping charges, in particular electrons, refer to charges jumping between lattice sites that contribute to conductivity and permittivity [24, 25, 31, 36, 55, 67, 77, 79, 81, 84]. Hopping conduction can be identified by a characteristic power-law function for conductivity σ_1 as a function of frequency ν: $\sigma_1 = \sigma_0 \nu^s$, $s < 1$. (Note: This power law is called the "Universal Dielectric Response" or UDR because of its wide (universal) applicability.) Applying the Kramers-Kronig relationships gives $\sigma_2 = \tan\left(\frac{s\pi}{2}\right)\sigma_0\nu^s$. We have $\varepsilon_1 = \frac{\sigma_2}{2\pi\nu\varepsilon_0}$ and substituting for σ_2 we get $\varepsilon_1 = \left(\frac{1}{2\pi\nu\varepsilon_0}\right)\left(\tan\left(\frac{s\pi}{2}\right)\sigma_0\nu^s\right) = \left(\frac{\tan\left(\frac{s\pi}{2}\right)\sigma_0}{2\pi\varepsilon_0}\right)\left(\nu^{s-1}\right)$. For $s < 1$,$\tan\left(\frac{s\pi}{2}\right) < \infty$; so $\varepsilon_1 \propto \nu^{s-1}$. Since $s < 1$,$\varepsilon_1 \propto \frac{1}{\nu^{1-s}}$ and so ε_1 can reach colossal values as $\nu \to 0$, i.e. for low frequencies. Electron hopping has been suggested [78] to occur in $Ti_{1-x}Nb_xO_2$ [67], $CaCu_3Ti_4O_{12}$ [31, 79], $BaTiO_3$ [24], and $La_{1-x}Bi_xMnO_3$ [55]. In a limiting case, the hopping electrons may become localized, i.e. pinned, to lattice defects leading to giant dipoles [1].

In another limiting case, where the material is a strongly disordered material (e.g. glass) with localized charge carrier states and held at low temperature, the variable range hopping (VRH) model can be applied. Variable range hopping implies a conductivity equation of the form $\sigma(\omega,T) = \sigma_0(\omega,0) + \sigma_1 \exp\left[-\left(\frac{T_0}{T}\right)^{\frac{1}{4}}\right]$ [85]. The signature feature is the temperature dependence of the conductivity. Krohns et al. [36] and Zhang and Tang [31] found the VRH model consistent with the data from experiments on CCTO.

Lattice-Pinned Electrons

As mentioned earlier in an extreme case hopping electrons may become almost immobile by being pinned to lattice sites. This effect can be exploited to produce CP material with low dielectric loss. In fact, [1] report a new line of research in which they theorize the possibility to create a material in which mobile ("hopping") electrons are localized ("pinned") to lattice sites by purposely designed lattice defects. These lattice-pinned electrons are able to move farther than atomically pinned electrons and therefore the induced dipole moment is larger than that of atomic dipoles i.e. the lattice-pinned electrons give rise to giant dipoles. Since the electrons are pinned, they are unable to freely "hop" throughout the lattice. This effectively lowers the conductivity of the material and therefore lowers dielectric loss. Therefore, according to this theory, the result of giant dipoles will be high-performance CP materials and the result of pinning will be low dielectric loss.

Hu et al. [1] showed that co-doping rutile TiO_2 with equal amounts of Nb (a donor) and In (an acceptor) increased the permittivity below 1MHz. The co-doping, which means doping with equal concentrations of donors and acceptors, is essential as the Nb assists in creating mobile electrons and the In assists in localizing those electrons. In addition, the material also showed low dielectric loss over a wide temperature range from 80 up to 450 K and over a broad frequency range. For example, $Nb + In$ co-doping at 0.05% results in room-temperature permittivity as high as $\approx 2 \cdot 10^4$, the dielectric loss is less than 0.05, and the frequency range is 10^1 to 10^5 Hz. They claim the observed, room-temperature CP behavior is not a result of Maxwell-Wagner (M-W) polarization in line with the theory behind the fabrication of this CP material. On the other hand, other workers claim that contact effects strongly affected Hu et al.'s measurements [13, 16] and that the defect dipole mechanism may not be the explanation for the measured giant ε_1.

A conventional cell of the rutile crystal structure is shown in figure 1.3.1. Ti atoms occupy the vertices and body center of the tetragonal cell and oxygen atoms occupy interior locations of the cell. In or Nb doping replaces the Ti atoms. It is noteworthy that the doping does not fracture the lattice into separate physical domains where boundary layer M-W effects would arise. The crystal structure resulting from the doping is shown in figure 1.3.2.

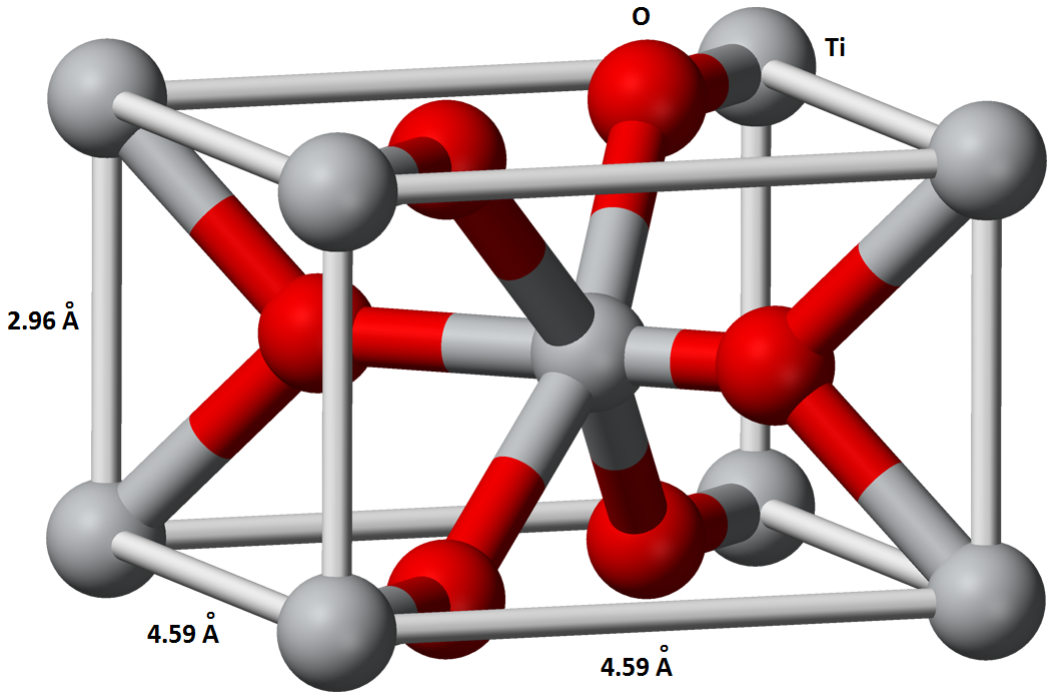

Figure 1.3.1: Crystal Structure of rutile TiO_2.
Modified from original image by B. Mills, 2007.
download from URL https://en.wikipedia.org/wiki/File:Rutile-unit-cell-3D-balls.png
Crystal dimensions from [20]

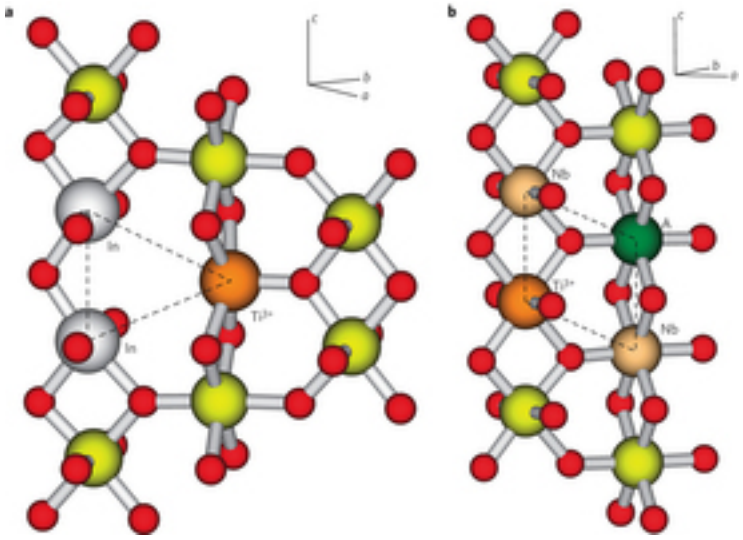

Figure 1.3.2: Nb and In doped rutile TiO_2. From [1]

The the importance of Hu's work extends beyond simply fabricating a CP material with

low dielectric loss. For instance, TiO_2 is a simple metal oxide and may be a representative of a large group of metal oxides in which high-performance CP behavior can be manufactured. Changing the dopants is another possibility. Preliminary studies show that Al^{3+} instead of In^{3+} co-doping also results in CP behavior. TiO_2 is abundant and has low toxicity, which makes it highly attractive as a base host material for commercial use. For full details of the fabrication methodology and experiments see [1].

1.4 Previous Work on Infrared Active Modes in Rutile

TiO_2 (rutile) has a tetragonal unit cell which has D_{4h} symmetry [86] (see fig. 1.3.1). The D_{4h} symmetry properties of rutile can be used to derive which vibrational modes are infrared active [87]. Since there are two formula units per unit cell, the total number of vibrational degrees of freedom is 18 (6 atoms $\times$ 3 degrees_of_freedom /atom). Three of these modes are acoustic, while the other 15 are optical.

It is shown in Gervais et al. [87], that the IR active modes are $3E_u + A_{2u}$ which means that up to three modes should be seen in spectra with incident electric field polarized perpendicular to the c-axis and only one mode should be seen with incident light polarized parallel to c-axis. The normal modes of vibration of the molecule come from the vibration of the atoms of the molecule about their equilibrium position in the lattice; bulk translations and rotations of the molecule are ignored. Infrared radiation excites the dipole moments. Dipoles involve the spatial displacement of charge where 3-dimensional displacement involves the three coordinate functions (x, y, z). A detailed explanation of the application of group theory to solids is in [86, 88].

Gervais and Piriou [87] explored the A_{2u} and E_u vibrational modes of TiO_2 as a function of temperature. In fig. 1.4.1 the A_{2u} reflectance spectrum was measured with the incident field polarized parallel to the c-axis, while the E_u spectrum was measured with incident field polarized perpendicular to c-axis. An extra mode of small oscillator strength is observed at about the same frequency (570 cm^{-1}) in both polarizations (see fig. 1.4.1). Gervais and Piriou [87] suggest that this might be either impurity related or a 2-phonon process. Doping causes some Ti atoms to be substituted with In or Nb. In the doped crystal the position of O atoms remains the same and the basic symmetry of rutile is preserved. It is expected that co-doped rutile will show similar temperature-dependent A_{2u} and E_u vibrational modes.

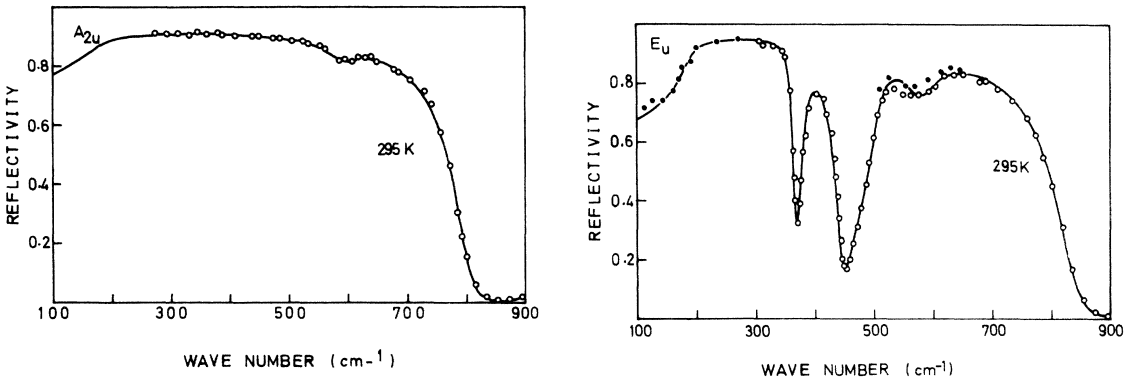

Figure 1.4.1: Reflectivity data for A_{2u} and E_u type modes at room temperature.
Left: Figure 2 from [87] showing reflectivity data for the A_{2u} type mode at room temperature (open circles) as well as the best fit data using the factorized model (full curve).
Right: Figure 3 from [87] showing reflectivity data for the E_u type mode at room temperature (open circles), data from Spitzer et al. (solid circles) as well as the best fit data using the factorized model (full curve).

Matsumoto et al. [89] studied the dielectric response of single crystal rutile and polycrystalline, ceramic TiO_2 at 300K. They used the four-parameter factorized form (see section 2.3) of the dielectric function to model the data because there is a large difference between the transverse optical (TO) and longitudinal optical (LO) mode frequencies. When this occurs the Drude-Lorentz model does not provide good fits and the four-parameter factorized model is appropriate. It is presumed that in polycrystalline ceramics the contributions of the A_{2u} and E_u vibrational modes will both be excited. Therefore, the bulk permittivity will be a combination of the permittivity of a single crystal in all three dimensions. In the simplest approximation, this means the permittivities parallel to the c-axis and perpendicular to the c-axis are combined in a weighted average. The weights are the ratio 1:2 where 1 corresponds to the one axis along which the A_{2u} mode can occur and 2 corresponds to the two axes along which E_u modes can occur. Figure 1.4.2 (figure 3. in [89]) shows excellent agreement between a three-oscillator version of the factorized model and the data for a polycrystalline sample.

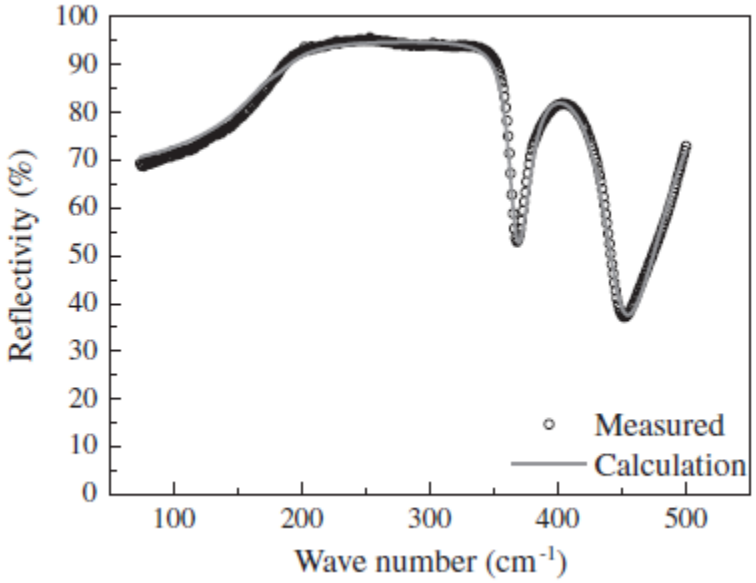

Figure 1.4.2: Reflectance Spectrum of Polycrystalline TiO_2. Figure 3. in Matsumoto et al. [89].

1.5 Plan of this Thesis

The purpose of this thesis is to investigate further the dielectric properties and especially the IR active modes of (Nb, In) co-doped TiO_2.

There are many different techniques to measure the dielectric function at different frequency ranges: capacitance spectroscopy in audio frequency to 1MHz range, co-axial reflection spectroscopy in the 1 MHz to 10 GHz range, THz transmission spectroscopy in the 0.15 to 1.5 THz range (5-50 cm^{-1}), and infrared reflectance spectroscopy in the 50 -10000 cm^{-1} part of the electromagnetic spectrum. Infrared reflectance spectroscopy provides a method to measure permittivity without using physical electrical contacts. The work done in this thesis involves reflectance spectroscopy measurements on $(Nb + In)$ co-doped rutile. The purpose of this thesis is to determine the contribution of transverse optic phonons to the low frequency dielectric function and to observe how co-doping affects the phonon contribution to the low frequency dielectric function.

Normal reflectance measurements were performed on polycrystalline samples of 0%, 5%, and 10% In and Nb co-doped TiO_2. The incident EM radiation stimulates phonons in the crystal lattice. Two forms of analysis of the reflectance data will be used: (i) the factorized form of the dielectric function will be used to fit the reflectance data (ii) Kramers-Kronig analysis will be performed and compared with the fits to the factorized form of the

dielectric function.

Chapter two will discuss the dielectric function models, optical conductivity and Maxwell's equations. Chapter three will discuss the materials and methods used to synthesize the co-doped TiO_2 ceramics. Chapter four will present the reflectance measurements and analysis including calculations of the conductivity and permittivity. Finally chapter five will conclude this thesis.

Chapter 2

Dielectric Function Models

2.1 Connection Between Dielectric Function and Optical Conductivity from Maxwell's Equations

The frequency dependent dielectric function $\tilde{\varepsilon}(\omega)$ is related to Maxwell's equations. In the following argument, we are assuming that the dielectric function $\varepsilon = \varepsilon_1 + i\varepsilon_2$ is a frequency dependent function.

Decouple Maxwell's equations by taking the cross product of the gradient of the electric field

$$\nabla \times (\nabla \times \vec{E}) = -\frac{\partial}{\partial t}(\nabla \times \vec{B}) \tag{2.1.1}$$

$$\nabla(\nabla \cdot \vec{E}) - \nabla^2 \vec{E} = -\frac{\partial}{\partial t}(\mu \vec{J}) + \mu \varepsilon_o \varepsilon_1 \frac{\partial \vec{E}}{\partial t} \tag{2.1.2}$$

but $\nabla \cdot \vec{E} = \frac{\rho}{\varepsilon_\circ} = 0$ then

$$\nabla^2 \vec{E} = \mu \sigma_1 \frac{\partial \vec{E}}{\partial t} + \mu \varepsilon_o \varepsilon_1 \frac{\partial^2 \vec{E}}{\partial t^2} \tag{2.1.3}$$

$\vec{E} = \tilde{\mathrm{E}}\hat{\varepsilon} e^{i(\hat{k}z - \omega t)}$ differentiating with respect to time gives $\Longrightarrow$ $\frac{\partial}{\partial t} \to -i\omega$

$$\begin{aligned} \frac{\partial^2 E}{\partial t^2} &= \frac{\partial}{\partial t}\left(\frac{\partial E}{\partial t}\right) = -i\omega \frac{\partial \vec{E}}{\partial t} \\ \frac{1}{-i\omega}\frac{\partial^2 E}{\partial t^2} &= \frac{\partial \vec{E}}{\partial t} \end{aligned}$$

and substituting the above into eq. 2.1.3 gives

$$\nabla^2 \vec{E} = \mu \varepsilon_o \left(\varepsilon_1 + i\frac{\sigma_1}{\varepsilon_o \omega}\right) \frac{\partial^2 \vec{E}}{\partial t^2} \tag{2.1.4}$$

one can see that the real part of the optical conductivity $\sigma = \sigma_1 + i\sigma_2$ is related to the

imaginary part of the dielctric function as follows:

$$\sigma_1 = \varepsilon_o \omega \varepsilon_2$$

Alternatively $\nabla^2 \vec{E}$ is proportional to the first time derivative, showing that ε_1 is related to σ_2.

$$\nabla^2 \vec{E} = \mu \frac{\partial \vec{E}}{\partial t} (\sigma_1 - i\omega\varepsilon_o\varepsilon_1) \tag{2.1.5}$$

2.2 Drude-Lorentz model for $\varepsilon(\omega)$

In the Drude-Lorentz model for $\varepsilon(\omega)$, one considers a solid to be a collection of non-interacting dipole oscillators. The spring constants and masses of these oscillators are different and depend on the physical process (absorption of radiation by optical phonons, or transitions between atomic states, or absorption by free carriers which would not have a spring force term (-kx)).

Consider one such dipole, modeled as a damped simple harmonic oscillator where the applied electric field is parallel to $\hat{x}$

$$\sum \vec{F} = m\vec{a} \tag{2.2.1}$$

$$qE - kx - \Gamma m \frac{dx}{dt} = m \frac{d^2x}{dt^2} \tag{2.2.2}$$

$$m \frac{d^2x}{dt^2} + \Gamma m \frac{dx}{dt} + kx = qE \tag{2.2.3}$$

$$m \frac{d^2x}{dt^2} + \Gamma m \frac{dx}{dt} + kx = q\tilde{E} e^{-i\omega t} \tag{2.2.4}$$

Where qE is the Coulomb force, kx is the Hooke's law spring force and $\Gamma m \frac{dx}{dt}$ is the drag.

Assume $x = \tilde{x} e^{-i\omega t}$ then $\frac{d}{dt} = -i\omega t$ and $\frac{dx}{dt} = \tilde{x}(-i\omega) e^{-i\omega t}$. Denote the natural, undamped frequency of the simple harmonic oscillator as $\omega_\circ$, also known as the resonant frequency. $m\omega_\circ^2$ is another way of expressing the spring constant k.

$$m\frac{d^2x}{dt^2}+\Gamma m\frac{dx}{dt}+m\omega_\circ^2 x = q\tilde{E}e^{-i\omega t} \quad (2.2.5)$$

$$m\tilde{x}(-i\omega)^2e^{-i\omega t}+\Gamma m\tilde{x}(-i\omega)e^{-i\omega t}+m\omega_\circ^2\tilde{x}e^{-i\omega t} = q\tilde{E}e^{-i\omega t} \quad (2.2.6)$$

$$-m\tilde{x}\omega^2-i\Gamma m\tilde{x}\omega+m\omega_\circ^2\tilde{x} = q\tilde{E} \quad (2.2.7)$$

Rearrange to solve for $\tilde{x}$

$$\tilde{x} = \frac{q\tilde{E}}{-m\omega^2-i\Gamma m\omega+m\omega_\circ^2} \quad (2.2.8)$$

$$= \frac{q\tilde{E}}{m[(\omega_\circ^2-\omega^2)-i\omega\Gamma]} \quad (2.2.9)$$

Recall the dipole moment $\vec{p}=\tilde{x}q\hat{x}$ and

$$\text{Polarization} = \sum\frac{\vec{p}_i}{V} \quad (2.2.10)$$

$$= \frac{Nq^2\tilde{E}\hat{x}}{m[(\omega_\circ^2-\omega^2)-i\omega\Gamma]} \quad (2.2.11)$$

where N is the number of dipole moments in the volume V

$$\vec{P}=\chi_e\varepsilon_\circ\vec{E}=\frac{Nq^2\tilde{E}\hat{x}}{m[(\omega_\circ^2-\omega^2)-i\omega\Gamma]} \quad (2.2.12)$$

assume $\vec{P}$ is in the x direction and recalling that $\vec{E}$ is parallel to $\hat{x}$, then

$$\chi_e=\frac{Nq^2}{m\varepsilon_\circ[(\omega_\circ^2-\omega^2)-i\omega\Gamma]} \quad (2.2.13)$$

the complex permittivity $\tilde{\varepsilon}=\varepsilon_\circ(\varepsilon_1+i\varepsilon_2)=\varepsilon_\circ(1+\chi_e)$ the dielectric constant is $\varepsilon_r=(1+\chi_e)$ and the electric displacement $\vec{D}=\varepsilon_\circ\vec{E}+\vec{P}=\varepsilon_\circ(1+\chi_e)\vec{E}_e$ and calling $\frac{Nq^2}{m}=\omega_p^2$

$$\tilde{\varepsilon} = 1+\frac{\omega_p^2}{(\omega_\circ^2-\omega^2)-i\Gamma\omega} \quad (2.2.14)$$

$$= 1+\frac{\omega_p^2[(\omega_\circ^2-\omega^2)+i\Gamma\omega]}{[(\omega_\circ^2-\omega^2)-i\Gamma\omega][(\omega_\circ^2-\omega^2)+i\Gamma\omega]} \quad (2.2.15)$$

$$= 1+\frac{\omega_p^2(\omega_\circ^2-\omega^2)+i\Gamma\omega\omega_p^2}{(\omega_\circ^2-\omega^2)^2+(\Gamma\omega)^2} \quad (2.2.16)$$

where the real part is

$$\varepsilon_1 = 1 + \frac{\omega_p^2(\omega_\circ^2 - \omega^2)}{(\omega_\circ^2 - \omega^2)^2 + (\Gamma\omega)^2} \tag{2.2.17}$$

and the imaginary part is

$$\varepsilon_2 = \frac{\Gamma\omega\omega_p^2}{(\omega_\circ^2 - \omega^2)^2 + (\Gamma\omega)^2} \tag{2.2.18}$$

and the plasma frequency $\omega_p^2 = \frac{Nq^2}{m\varepsilon_\circ}$ is for one Lorentz oscillator. This can be generalized to multiple oscillators. ε_∞ represents the contribution from the bound electrons to the dielectric function and is sometimes referred to as ε_{core}.

$$\tilde{\varepsilon}(\omega) = \varepsilon_\infty + \sum_j^n \frac{\omega_{pj}^2}{(\omega_{\circ j}^2 - \omega^2) - i\Gamma_j\omega} \tag{2.2.19}$$

$$\varepsilon_1(\omega) = \varepsilon_\infty + \sum_j^n \frac{\omega_{pj}^2(\omega_{\circ j}^2 - \omega^2)}{(\omega_{\circ j}^2 - \omega^2)^2 + (\Gamma_j\omega)^2} \tag{2.2.20}$$

$$\varepsilon_2(\omega) = \sum_j^n \frac{\Gamma\omega\omega_{pj}^2}{(\omega_{\circ j}^2 - \omega^2)^2 + (\Gamma_j\omega)^2} \tag{2.2.21}$$

2.3 Factorized Model

It is found that the Drude-Lorentz model of the dielectric function fails for materials that exhibit wide bands. “Wide” is meant to describe a band in which there are definite left and right shoulders to the peak. For such materials, Gervais and Piriou apply [87] the four parameter semiquantum model in the form of a factorized form of the dielectric function.

$$\tilde{\varepsilon}(\omega) = \varepsilon_\infty \prod_j^n \frac{\omega_{Lj}^2 - \omega^2 - i\Gamma_{Lj}\omega}{\omega_{Tj}^2 - \omega^2 - i\Gamma_{Tj}\omega} \tag{2.3.1}$$

where L denotes the longitudinal modes and T denotes the transverse modes.

The zeroes of the dielectric function occur at the longitudinal frequencies ω_{Lj} [76]. This result can be derived as follows [90]. Recall for a homogeneous, linear insulator.

$$\begin{aligned} \textit{Linear} \Rightarrow \qquad \vec{D} &= \varepsilon(\omega)\vec{E} && (2.3.2)\\ \nabla\cdot\vec{D} &= \nabla\cdot\varepsilon(\omega)\vec{E} && (2.3.3)\\ &= \varepsilon(\omega)\nabla\cdot\vec{E} && (2.3.4)\\ \textit{Insulator} \Rightarrow \quad \varepsilon(\omega)\nabla\cdot\vec{E} &= 0 && (2.3.5) \end{aligned}$$

$\nabla\cdot\vec{D}=0$ because of macroscopic charge neutrality. The longitudinal electric field that is due to the oscillation of charged ions is parallel to the wave vector. Consider the plane wave

$$\vec{E}(\vec{r},t)=\vec{E}_0\exp\left[i\left(\vec{k}\cdot\vec{r}-\omega t\right)\right] \tag{2.3.6}$$

Since $\vec{E}$ is parallel to $\vec{k}$ in a longitudinal mode then $\vec{k}\cdot\vec{E}\neq 0$ and therefore $\nabla\cdot\vec{E}\neq 0$. Therefore, the previous result that $\varepsilon(\omega)\nabla\cdot\vec{E}=0$ implies that $\varepsilon(\omega)=0$ for longitudinal mode oscillations.

Now consider the factored-form equation for the dielectric function. For small values of Γ_{Lj}, $\tilde{\varepsilon}$ is approximately

$$\tilde{\varepsilon}(\omega)\simeq\varepsilon_\infty\prod_j^n\frac{\omega_{Lj}^2-\omega^2}{\omega_{Tj}^2-\omega^2-i\Gamma_{Tj}\omega} \tag{2.3.7}$$

Thus, $\tilde{\varepsilon}\left(\omega_{Lj}\right)=0$ for all j. That is, the longitudinal frequencies are the zeroes of the factored-form of the dielectric function. This supports the idea that the numerator of the factored form of the dielectric function describes the behavior of the longitudinal modes.

2.4 Determination of the Dielectric Function from Reflectance Data

The optical response function $\widetilde{\varepsilon}(\omega)\equiv\varepsilon_1(\omega)+i\varepsilon_2(\omega)$ has many interchangeable forms including the optical conductivity and the complex index of refraction $\widetilde{N}(\omega)\equiv n(\omega)+i\kappa(\omega)$ which is the square root of the complex dielectric function. The fraction of light reflected (R) is a function of the index of refraction as will be shown below.

$$\widetilde{E}_{Reflect}(\omega) \equiv r(\omega) e^{i\theta(\omega)} \widetilde{E}_{Incident}(\omega) \tag{2.4.1}$$

$$\widetilde{r}(\omega) \equiv r(\omega) e^{i\theta(\omega)} \tag{2.4.2}$$

$$R(\omega) = \frac{Intensity_{Reflect}}{Intensity_{Incident}} = \frac{|\widetilde{E}_{Reflect}(\omega)|^2}{|\widetilde{E}_{Incident}(\omega)|^2} = r(\omega)^2 \tag{2.4.3}$$

It is possible to determine the complex dielectric function $\varepsilon(\omega)$ from normal incidence reflectance data.

The phase information $\theta(\omega)$ appears to be lost because $\theta(\omega)$ is not measured. However, $\theta(\omega)$ can be retrieved indirectly by using the Kramers-Kronig relations. It can be shown [90] that for any $\omega_0 > 0$

$$\theta(\omega_0) = \frac{\omega_0}{\pi} P \int_0^\infty \frac{\ln R(\omega) - \ln R(\omega_0)}{\omega_0^2 - \omega^2} d\omega \tag{2.4.4}$$

The integrand has a singular point at ω_0 which lies in the range of integration. Therefore it is necessary to use a Cauchy Principal Value (CPV) to evaluate this improper integral. The CPV is denoted with a "P" prefix to the integral sign.

The difficulty using this equation is that $R(\omega)$ is measured over a finite range. A practical application of the equation means that $R(\omega)$ must be extrapolated outside the range of measurements.

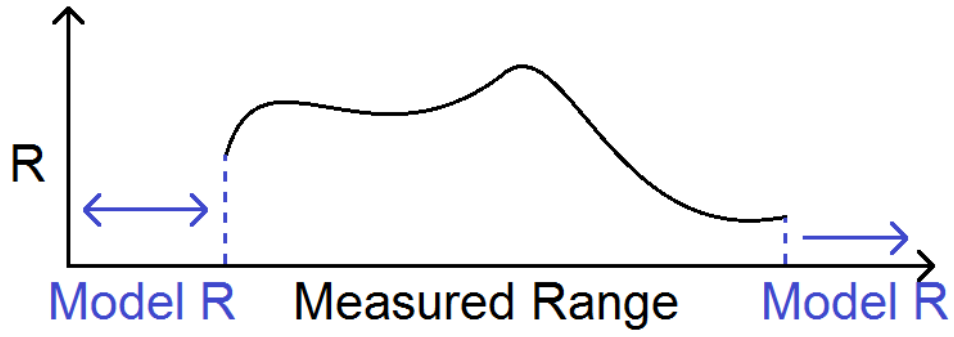

Figure 2.4.1: The measured frequency range is finite. Reflectance must be modeled to complete the spectrum over a wider range of frequencies.

The procedure to calculate an approximation for $\varepsilon_1(\omega)$ and $\varepsilon_2(\omega)$ in terms of reflectance data is

(1) measure $R(\omega)$ on a finite range of ω

(2) approximate $R(\omega)$ on the interval $[0,\infty)$ by extrapolating $R(\omega)$ outside the measured range

(3) calculate $r(\omega) = \sqrt{R(\omega)}$

(4) calculate $\theta(\omega)$ using the Kramers-Kronig relations

(5) calculate $n(\omega)$ and $\kappa(\omega)$ in terms of $r(\omega)$ and $\theta(\omega)$

$$n(\omega) = \frac{1-r^2}{1+r^2-2r\cos\theta} \tag{2.4.5}$$

$$\kappa(\omega) = \frac{2r\sin\theta}{1+r^2-2r\cos\theta} \tag{2.4.6}$$

which follows from the relation

$$\frac{\widetilde{E}_{Reflect}}{\widetilde{E}_{Incident}} = \frac{\widetilde{N}-1}{\widetilde{N}+1} = re^{i\theta} \tag{2.4.7}$$

(6) calculate $\varepsilon_1(\omega)$ and $\varepsilon_2(\omega)$

$$\varepsilon_1(\omega) = n^2-\kappa^2 \tag{2.4.8}$$

$$\varepsilon_2(\omega) = 2n\kappa \tag{2.4.9}$$

which follows from the relation

$$\widetilde{N}(\omega) = \sqrt{\widetilde{\varepsilon}(\omega)} \tag{2.4.10}$$

Another way to determine $\varepsilon_1(\omega)$ and $\varepsilon_2(\omega)$ from $R(\omega)$ is by doing a least squares fit of a model of $R(\omega) = f(\varepsilon_1(\omega),\varepsilon_2(\omega))$, where $\widetilde{\varepsilon}(\omega) = \varepsilon_1(\omega) + i\varepsilon_2(\omega)$ is either the Drude-Lorentz model (Eq. 2.2.19) or the factorized model (Eq. 2.3.1).

The Fresnel equations for radiation at a normal angle of incidence are

$$R = \left|\frac{\sqrt{\widetilde{\varepsilon}}-1}{\sqrt{\widetilde{\varepsilon}}+1}\right|^2 \tag{2.4.11}$$

$$= \frac{|n+i\kappa-1|^2}{|n+i\kappa+1|^2} \tag{2.4.12}$$

relates the reflectance R and the dielectric function ε.

Chapter 3

Methods and Materials

3.1 Methods and Materials

All samples were made using standard solid state techniques using the materials TiO_2 in mixture of anatase and rutile (Alfa Aesar [1] product #10897), In_2O_3 (Alfa Aesar product #10709) and Nb_2O_5 (Alfa Aesar product #10822). This technique involves mixing separate materials in a mortar and pestle with a liquid such as methanol or acetone to keep the powder from escaping. Our goal was to co-dope TiO_2 with equal amounts of donor (Nb) and acceptor (In) substitutional impurities ($Ti_{1-2x}Nb_xIn_xO_2$). To determine the amount of each powder to mix the following calculation was made of the mass ratio of the starting chemicals

$$\frac{In_2O_3 \text{ or } Nb_2O_5}{TiO_2} = \frac{x}{2} * \frac{m(In_2O_3 \text{ or } Nb_2O_5)}{(1-2x)*79.87}$$

This ratio was calculated for all percent doping levels for both In_2O_3 and Nb_2O_5.

In this experiment methanol was used to keep all the powder inside the mortar. The powders were mixed by hand for a minimum of 30 minutes. Once the powders were thoroughly combined the mixture was left to dry. Once the mixture was dried approximately 0.6g of it was pressed in a laboratory hand press. The sample remained in the press for thirty minutes and was under at least 2.6 tonnes of pressure at all times. After this time the sample is removed and placed in an alumina crucible. There were 7 different soaking temperatures. They were 1000, 1100, 1200, 1300, 1400, 1450 and 1500 degrees celsius. Samples were soaked at one of the seven previous temperatures for 12 hours. This process was repeated multiple times to make the following different sample compositions: 100% TiO_2, 0.5 % In only; 0.5, 1, 5, and 10% Nb only; 0.5, 1, 5 and 10% co-doped. Selected co-doped samples were used in the XRD and reflectance experiments for further study.

[1] Alfa Aesar - A Johnson Matthey Co.; 30 Bond St.; Ward Hill, MA 01835 USA

3.2 X-Ray Diffraction

Samples fired at temperatures 1000, 1100, 1200, 1300, 1400 and 1500 were first examined using the precise powder sequence on the Rigaku SmartLab. This experiment showed the disappearance of all but the rutile phase in TiO_2 at 1400 degrees.

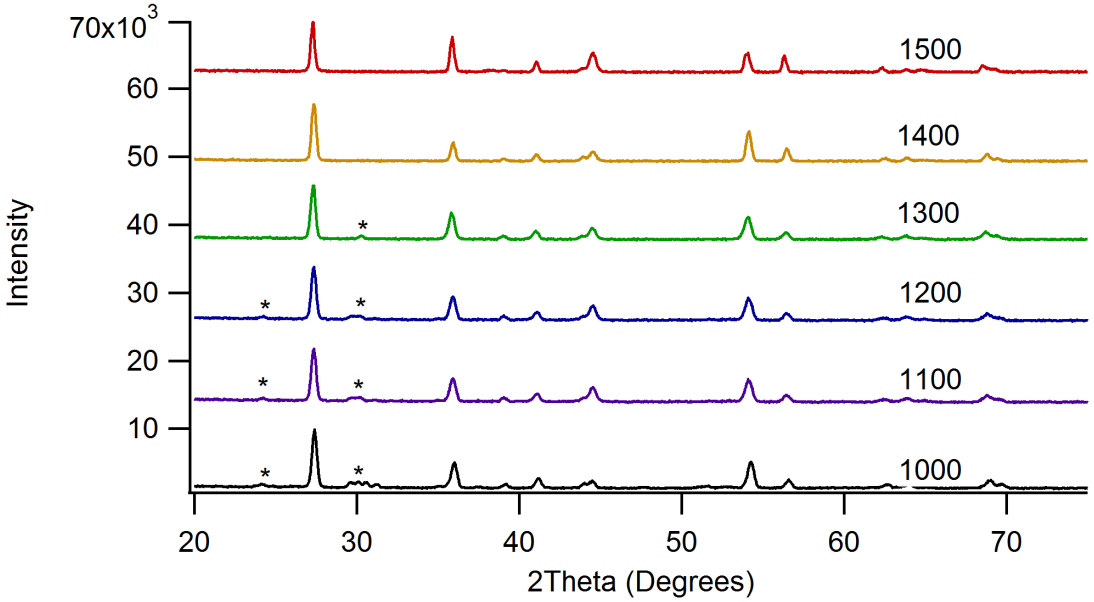

Figure 3.2.1: X-ray diffraction spectra of 10% co-doped TiO_2 sintered at temperatures 1000-1500 degrees Celsius in increments of 100 degrees. Asterisks (*) mark non-rutile phases. From [13].

Samples were placed on a small table that fits into the Rigaku X-Ray. Optical alignment was performed at the beginning of every X-Ray session. Sample measurements were then made using a preprogrammed set of instructions under the powder analysis option. Data was taken from 20 to 110 degrees. Data past 75 degrees is not shown here because there are no features to be seen.

3.3 Scanning Electron Microscope

Scanning electron microscope images were taken at the Canadian Center for Electron Microscopy of TiO_2 samples made at 1000°, 1300° and 1500° degrees (fig. 3.3.1). The images show the grain size at 1000 times magnification. As the sintering temperature increased there is a noticeable increase in grain size.

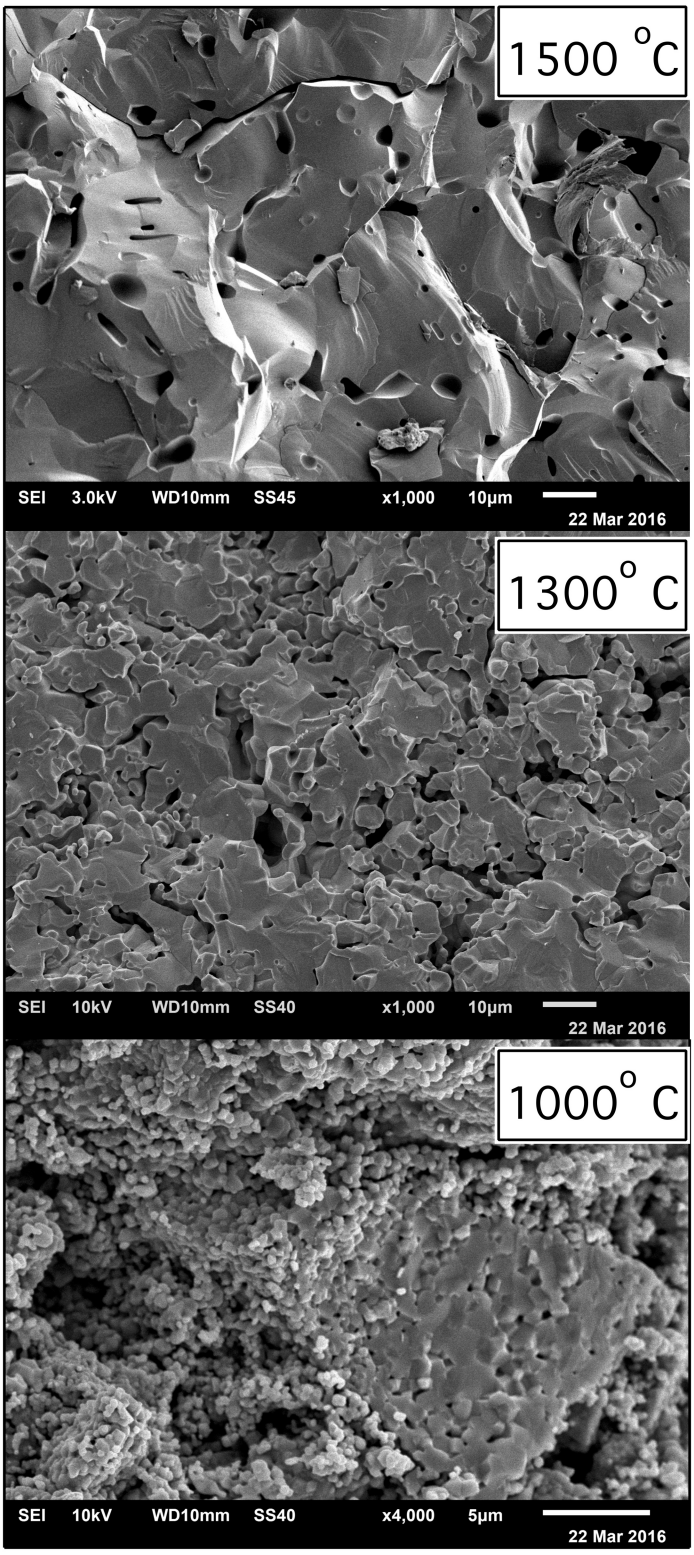

Figure 3.3.1: Microstructure of TiO_2 at 1000, 1300 and 1500 degrees Celsius. Images from [13]. Note: magnification at 1500 C and 1300 C is $\times$1000, magnification at 1000 C is $\times$4000.

3.4 Reflectance Spectra

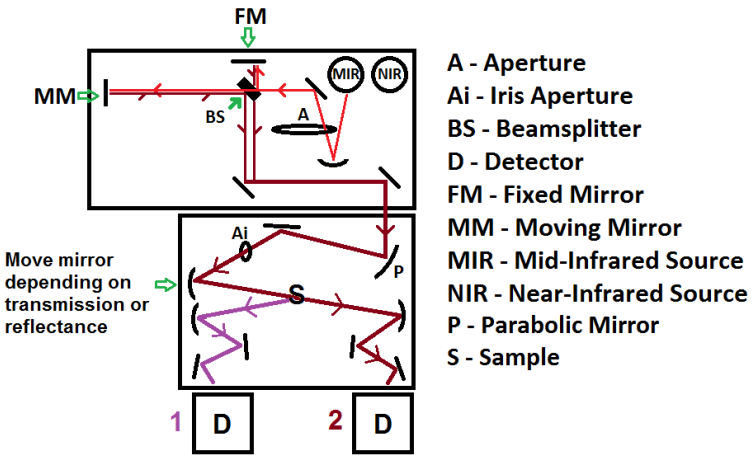

Figure 3.4.1: Schematic diagram of the optical setup in the lab. The upper box in the sketch represents the Bruker (Model IFS 66V/S) which contains the light sources and Michelson interferometer. The light rays are parallel as they emerge from the Michelson. The lower box in the sketch is a custom built unit through which the Janis cryostat which holds the sample traverses. The first mirror in the lower box is a parabolic mirror which focuses the light onto an iris aperture. A spherical mirror focuses the image of the illuminated iris onto the sample. Note that after the light reaches the sample there are two different optical paths which permit the measurement of reflectance or transmission. Position 1 on the schematic is for the reflectance setup. Position 2 is for transmission. The detector is moved depending on the desired data to be taken.

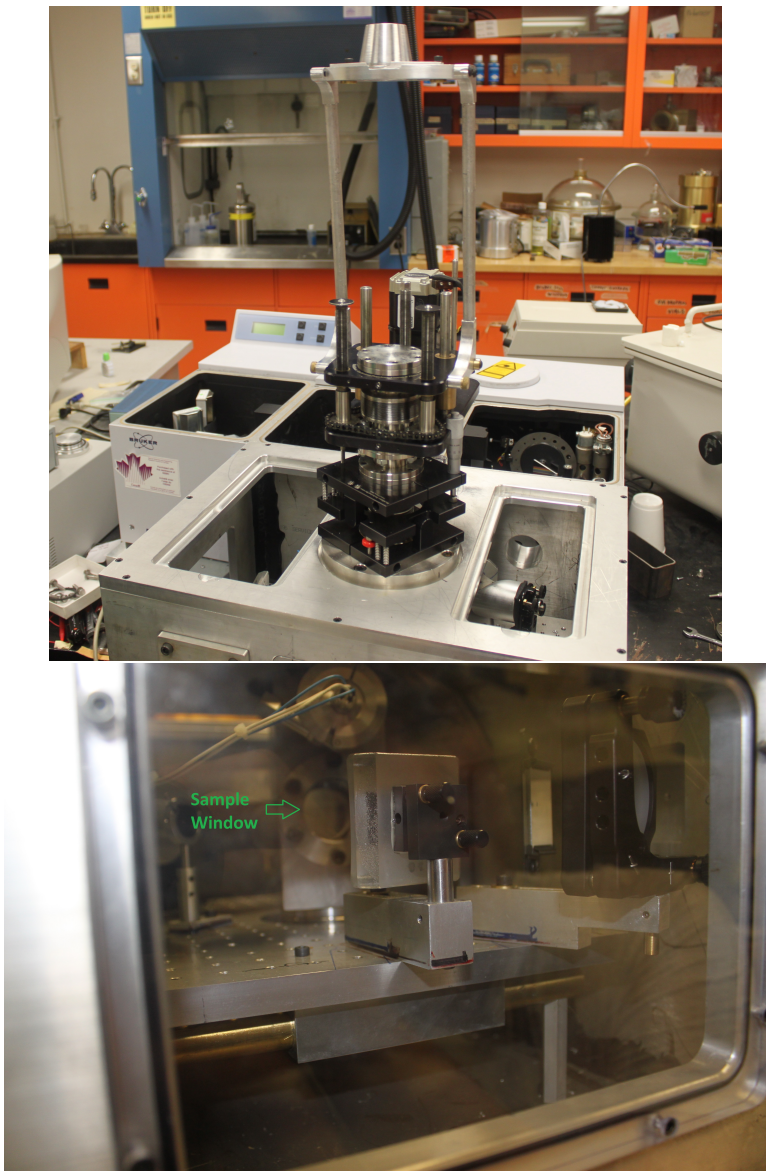

Figure 3.4.2: Photos of the optical setup in the lab showing the two boxes and the cryostat tower. The sample can be seen through a clear window on the side of the outerbox in the lower photograph.

Reflectance R is calculated with the equation (which is equivalent to equation 1 in [91])

$$R(\text{sample}) = (\frac{I_s}{I_r}) * [\frac{I_r(Au)}{I_s(Au)}] * R(Au) \tag{3.4.1}$$

where

I_r = intensity of reflected light from the reference mirror

I_s= intensity of reflected light from the sample

$I_r(Au)$= intensity of reflected light from the reference mirror when the sample is coated

with Au; this should equal I_r since the mirror has not been altered

$I_s(Au)$= intensity of reflected light from the sample after *in situ* gold evaporation onto the sample

$R(Au)$= reflectance of sample coated *in situ* with Au; this equals $I_s(Au)$

The purpose of taking ratios with respect to the reference mirror is to remove experimental effects due to the instrument e.g. effects from the reference mirror, changes in the electronics over the duration of the experiment [91].

Mid infrared and far infrared reflectance spectra were collected for pure TiO_2, 5% co-doped sintered at 1450° and 10% co-doped sintered at 1450° at temperatures from 4K to 300K. Samples were mounted onto small copper disks that were secured onto the cold finger of the Janis cryostat (position S in 3.4.1) that was equipped with heating wires and temperature sensors. This apparatus fit into the top of the reflectance and transmission setup. It is screwed tightly to secure its position. The signal from the sample is then maximized by slightly adjusting the reflecting mirrors. All samples were initially cooled to 4K then warmed to 300K. Gold was evaporated onto the surface after the 300K measurement was taken. An explanation of the gold evaporation technique appears in [91]. The sample was then remeasured at 300K and cooled to 4K again to retake the rest of the measurements. Each measurement also had multiple spectra taken. The final spectra were averages of these measurements. From this data the complex dielectric function can be obtained by either fitting to the factorized model of the dielectric function or Kramers Kronig analysis as discussed in Chapter 2 where reflectance is calculated by equation 3.4.1.

Chapter 4

Results and Discussion

The reflectance measurements were made with unpolarized light on polycrystalline samples and therefore all of the IR modes were sampled. The reflectance measurements were taken at resolution 4 cm^{-1}.

Consider the TiO_2 spectrum seen in figure 4.0.1. The data look quite similar to the single crystal E_u spectrum (see fig. 1.4.1). Note that only three bands (labelled 1, 2, and 3 in the top margin of the figure) plus the dip near 570–600 cm^{-1} (labelled w) at all temperatures can be seen. The reason why there isn't a fourth band is that the frequency and oscillator strength of the A_{2u} mode is quite similar to the lowest frequency E_u mode [87].

The spectrum for the CD 5% sample seen in figure 4.0.1 is also similar to the single crystal E_u TiO_2 spectrum. Note that only three bands can be seen. There is no fourth band as explained for the TiO_2 sample. The dip (w) near 570–600 cm^{-1} has become much more shallow and a new dip near 650 cm^{-1} has appeared except at 300 K. Bands 2 and 3 have become less reflective (reflectivity decreased) than in the TiO_2 sample, but the minimum value of the dip separating these two bands has become more reflective (reflectivity increased).

The spectrum for the CD 10% sample seen in figure 4.0.1 also has three bands. There is no fourth band as explained for the TiO_2 sample. The dip near 570–600 cm^{-1} has disappeared entirely and the dip near 650 cm^{-1} has become more pronounced. The dip now also appears at 300 K. As in the CD 5% sample, bands 2 and 3 have become less reflective (band 2 is noticeably less than the CD 5% value), but the minimum value of the dip separating these two bands has become more reflective (even more than the CD 5% values). The slope of the first band appears different than in the 5% co-doped and undoped samples.

The overall effect of co-doping is to make the sample less reflective and this effect is strongest in the region surrounding the second band. In the CD 10% sample this region looks like a dip in the spectrum.

For all levels of doping the first band is a mode that softens as can be seen by the temperature-dependent shift in the left edge of the band. The second and third bands do not shift significantly with decreasing temperature.

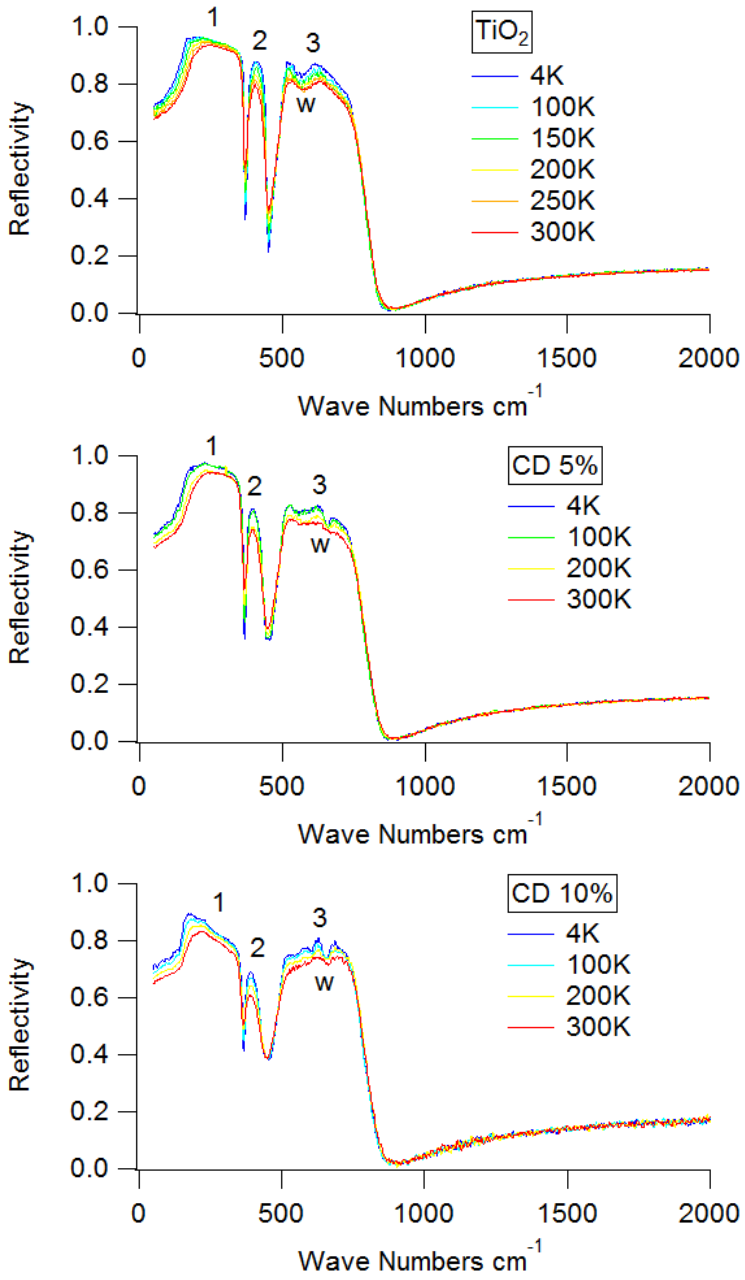

Figure 4.0.1: Reflectance spectra of TiO_2 co-doped at 0%, 5% and 10% levels. (Resolution = 4 cm^{-1})

Figure 4.0.2 shows the effect of co-doping on the reflectance at T=300K. The graph shows that co-doping only slightly changes the frequency of the bands. Co-doping at 5% has neglible effect on the reflectivity for the first band and a small effect on the second and third bands. Co-doping at 10% greatly reduces the reflectivity of the first and second bands from that of TiO_2 and CD 5%. At frequencies greater than 700 cm^{-1} the three graphs are co-incident; that is, co-doping has no effect.

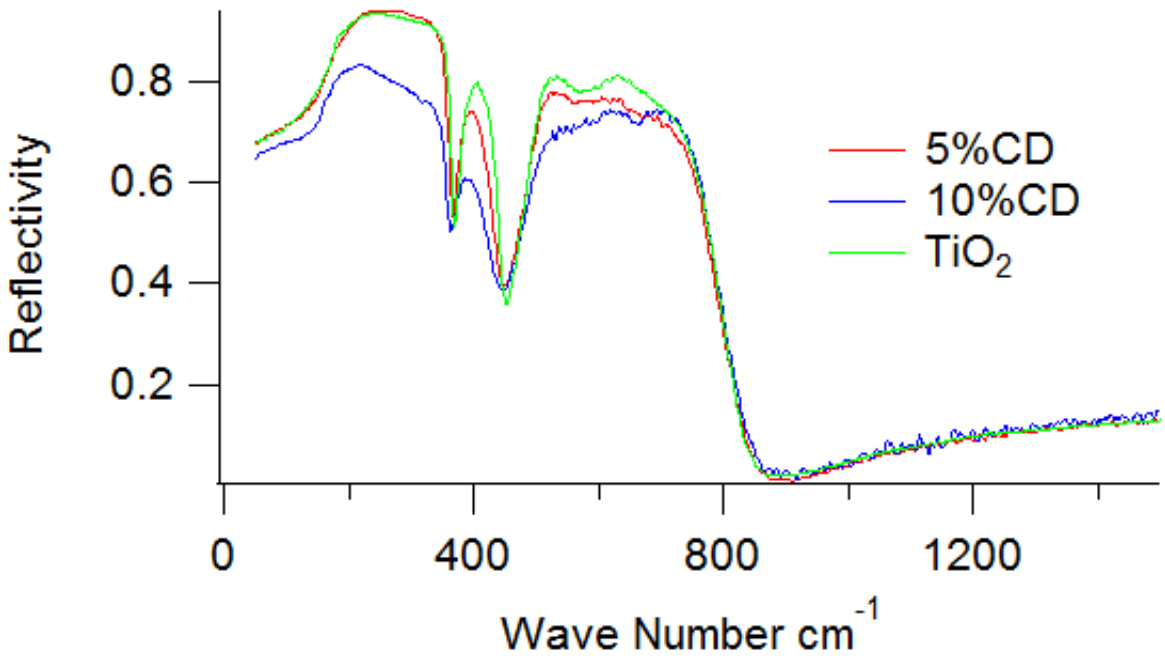

Figure 4.0.2: Effect of co-doping on the Reflectivity at T=300K

4.1 Determination of the Dielectric Function by fitting the Reflectance

The data were first analyzed using the Drude-Lorentz model, but the fits were not satisfactory. Fig. 4.1.1 shows the reason why. For a wide band, the fit to the four-parameter factorized model (eq. 4.1.1) is much better. This can be attributed to the fact that for each oscillator the factorized model has an extra degree of freedom over the Drude-Lorentz model.

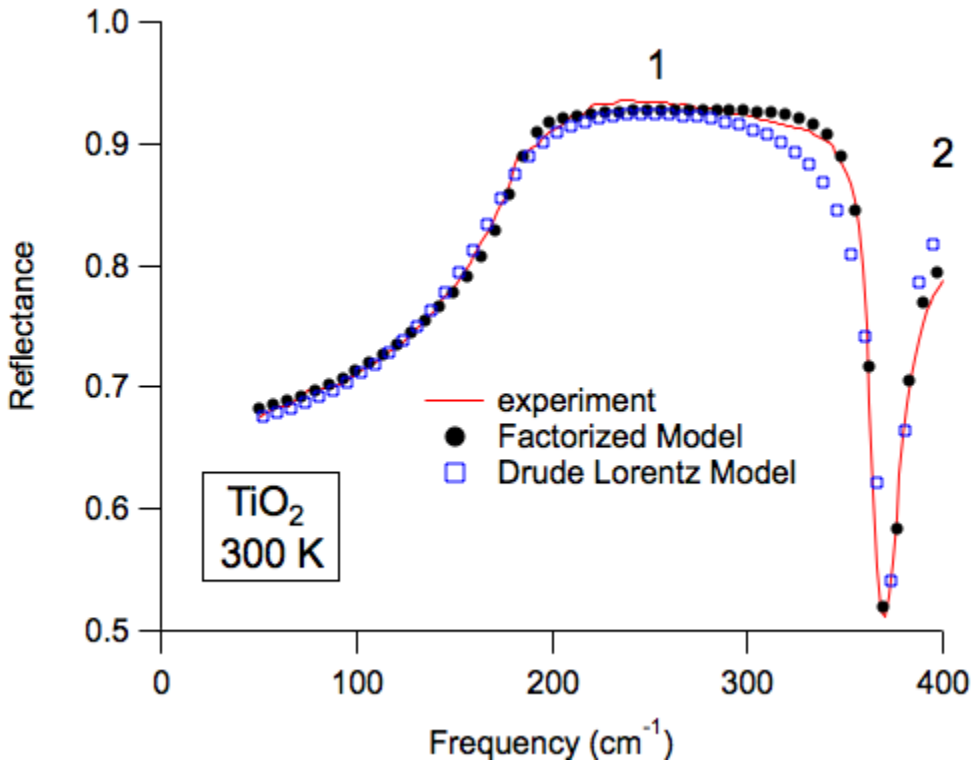

Figure 4.1.1: Experimental data is plotted with the factorized and Drude Lorentz model. The shoulder is slightly cutoff by the Drude model whereas the factorized model fits to the data better.

For polycrystalline samples, following [89], the dielectric function is fit using the factorized model. The E_u modes are perpendicular to the c-axis and the A_{2u} mode is parallel to the c-axis and will be labelled respectively as a1, a2, a3, a4 and c in tables 4.1.1, 4.1.2, and 4.1.3. The mode labelled "a4" in the tables is the the weak mode labelled "w" in fig. 4.0.1. Although single crystal data showed the extra mode (w) in both the a and c polarized spectra [87] for modelling purposes this work assumes the extra mode only perpendicular to c (ε_a). This is because the weak mode is approximately the same frequency in both polarizations and the data can be very well modeled near 570 cm^{-1} with a total of five oscillators rather than six. In other words, keeping all six modes would give too many degrees of freedom. Therefore, this work models ε_a with four oscillators (a1, a2, a3, a4) and ε_c with one oscillator (c). Equation 2.3.1 can be written for the E_u and A_{2u} modes as

$$\varepsilon_{a,c}(\omega) = \varepsilon_{\infty;a,c} \prod_i \frac{\omega_{LO_i}^2 - \omega^2 - i\Gamma_{LO_i}\omega}{\omega_{TO_i}^2 - \omega^2 - i\Gamma_{TO_i}\omega} \tag{4.1.1}$$

The bulk dielectric function is presumed to be a weighted, linear combination of the dielectric functions in a 2:1 ratio [89].

$$\varepsilon(\omega) = \frac{2}{3}\varepsilon_a + \frac{1}{3}\varepsilon_c \tag{4.1.2}$$

For the co-doped 5% and 10% samples the structure (weak dip) near 570 cm^{-1} (fig. 4.0.2) disappeared in the third band. Therefore, the four "a" oscillator model just described is changed to a three "a" oscillator model for the co-doped 5% and 10% samples. The structure of the third band is more complicated. This is better treated using Kramers-Kronig analysis which will be discussed below.

The fit of the factorized model was done using a function written within Igor Pro software. The parameters for fitting $\varepsilon(\omega)$ were found by non-linear least squares fitting (Levenberg-Marquardt algorithm) built into Igor Pro Software using Gervais and Piriou parameters [87] as a starting point. The fitted parameters of the factorized model appear in tables 4.1.1, 4.1.2, and 4.1.3. Fitting the parameters for the a4 mode gives a model in which the calculated dielectric is highly unreasonable. The reason for this behavior is unknown. Therefore, these parameters are omitted from further analysis. Some trends in the fitted parameters will be described next.

ω_{TO,a_1} increases with increasing temperature for all samples. Therefore, the "a1" oscillator corresponds to a phonon mode that softens. The transverse mode frequencies for a2 and a3 do not vary much as seen in fig. 4.1.3. This figure also shows that a4 appears to be softening but not as much as a1. The value of ω_{TO,a_1} is larger for the CD 10% sample at 300K. Similarly, the longitudinal mode frequencies for a2 and a3 do not vary much. ω_{LO,a_1} is approximately the same for TiO_2 and CD 5%. ω_{LO,a_1} for CD 10% is less than the values for TiO_2 and CD 5% except at 300K. This value is approximately the same as for TiO_2 and CD 5%.

$\omega_{LO,c}$ is approximately the same for TiO_2 and CD 5%. $\omega_{LO,c}$ for CD 10% is greater than the values for TiO_2 and CD 5% except at 300K. This value is approximately the same as for TiO_2 and CD 5%. At all temperatures ($\Gamma_{LO,c}$ for TiO_2) < ($\Gamma_{LO,c}$ for CD 5%) < ($\Gamma_{LO,c}$ for CD 10%), except for CD 10% at 300K. The value for CD 10% at 300K is approximately equal to the vaules for TiO_2 and CD5%. Overall, co-doping either increases or does not affect $\omega_{LO,c}$. However, co-doping does affect $\Gamma_{LO,c}$. Co-doping appears to affect the "c" oscillator more than the "a_1" oscillators.

Figure 4.1.2 overlays the softening-mode frequency (highly temperature-dependent, lowest frequency IR mode) determined by various experiments: single crystal IR reflectance from [87], neutron scattering [92], and inelastic x-ray scattering (IXS) [93] measurements of the transverse mode frequencies by reflectance fits. For the E_u mode at 300 K, this work's fit is in very good agreement with the IXS result and is lower than the neutron and

earlier IR results. For the A_{2u} mode, this work's fits are all greater than the neutron results, although the two sets agree reasonably well in the range 100-150 K and the trendlines for both sets are close to parallel. This work's fitted model relies on an estimate of ε which is a linear combination of ε_a and ε_c as measured on a ceramic pellet which is probably the reason for the discrepancy in measured frequencies. Since the frequencies of the ε_a and ε_c modes are different, adjusting the weights in the linear combination will cause a shift in the estimated frequency for ε. A similar statement can be made for the amplitude of ε. It is difficult to separate the two mode frequencies in polycrystalline reflectance data. On the other hand, Traylor et al. [92] made neutron scattering measurements on a single crystal of rutile.

Table 4.1.3 shows a splitting of the longtudinal and tranverse optic modes for the a_1 oscillator. The strength of the splitting is related to the plasma frequency. The strength of an IR mode is determined by the strength of the dipole. Hence, a stronger dipole will result in a stronger IR active mode. The Born effective charge changes as the dipole moment changes; that is, the Born effective charge will increase if the dipole moment (and corresponding strength of the IR active mode) increases.

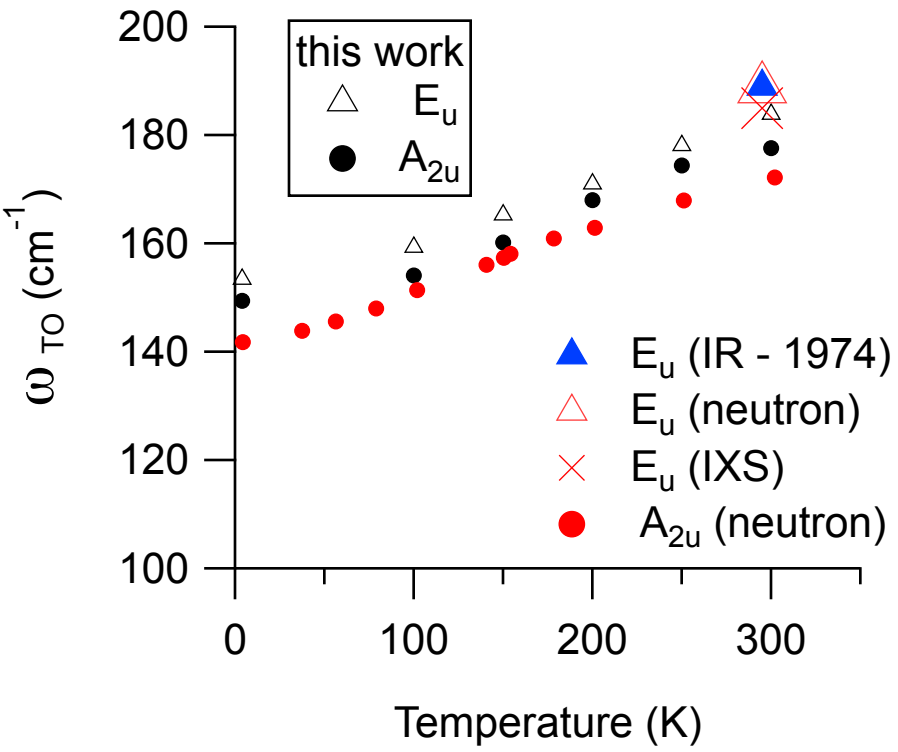

Figure 4.1.2: Comparison of the softening-mode transverse optical frequency (ω_{TO}) determined in the fits for TiO_2 to those determined by single crystal (IR) reflectance , neutron scattering, and inelastic x-ray scattering (IXS).
single crystal IR reflectance from [87]
neutron scattering from [92]
IXS from [93]

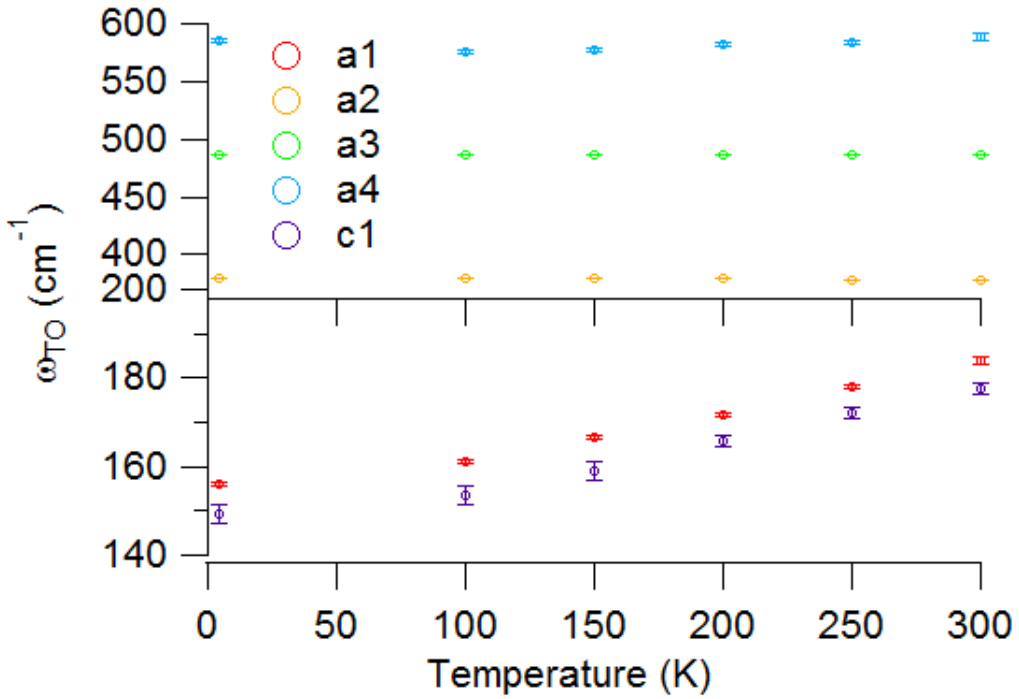

Figure 4.1.3: Transverse Mode Frequencies ω_{TO} vs. Temperature in TiO_2

	TiO2											
Temp. (K)	4K	4K	100K	100K	150K	150K	200K	200K	250K	250K	300K	300K
	Par	Unc	Par	Unc	Par	Unc	Par	Unc	Par	Unc	Par	Unc
number of a oscillators	4		4		4		4		4		4	
number of c oscillators	1		1		1		1		1		1	
$\varepsilon_{\infty,a}$	5.86	0.02	5.78	0.02	5.77	0.02	5.63	0.01	5.64	0.01	5.90	0.01
$\varepsilon_{\infty,c}$	7.68	0.03	7.70	0.03	7.72	0.03	7.74	0.02	7.77	0.02	7.77	0.03
ω_{TO,a_1}	156.0	0.5	161.1	0.5	166.6	0.5	171.9	0.4	178.0	0.4	183.9	0.6
Γ_{TO,a_1}	7.2	0.7	8.0	0.7	9.8	0.8	12.8	0.6	16.1	0.7	23	1
ω_{LO,a_1}	820.5	0.5	820.4	0.5	822.2	0.6	826.5	0.4	829.0	0.4	832.0	0.6
Γ_{LO,a_1}	49	1	51	1	55	1	51.4	0.9	56.6	0.9	66	2
ω_{TO,a_2}	380.5	0.1	380.4	0.1	380.0	0.2	379.6	0.1	378.4	0.2	378.1	0.3
Γ_{TO,a_2}	9.2	0.2	11.4	0.3	14.2	0.3	16.8	0.3	17.9	0.3	20.6	0.6
ω_{LO,a_2}	355.4	0.2	354.9	0.2	354.4	0.2	353.9	0.2	354.3	0.2	354.5	0.3
Γ_{LO,a_2}	0.0	0.3	0.0	0.4	0.0	0.4	0.0	0.3	0.0	0.2	2.3	0.5
ω_{TO,a_3}	487.4	0.2	486.4	0.2	486.6	0.3	486.4	0.2	486.3	0.2	486.7	0.3
Γ_{TO,a_3}	25.3	0.4	28.4	0.4	31.7	0.5	34.9	0.4	37.8	0.4	39.1	0.8
ω_{LO,a_3}	431.1	0.2	431.0	0.2	430.7	0.2	429.8	0.2	428.9	0.2	429.0	0.3
Γ_{LO,a_3}	7.2	0.3	9.3	0.3	13.25	0.4	17.2	0.3	21.4	0.4	26.0	0.6
ω_{TO,a_4}	585	2	577	2	577	2	583	2	584	1	589	3
Γ_{TO,a_4}	36	4	34	4	37	4	52	4	49	3	66	7
ω_{LO,a_4}	583	2	574	2	573	2	578	2	579	2	584	3
Γ_{LO,a_4}	40	5	35	4	37	4	53	4	50	3	69	8
$\omega_{TO,c}$	149	2	153	2	159	2	166	1	172	1	178	1
$\Gamma_{TO,c}$	58	1	61	1	64	1	67.6	0.9	71.2	0.9	74	1
$\omega_{LO,c}$	795.6	0.8	795.7	0.8	795.7	0.9	795.6	0.6	795.6	0.6	795	1
$\Gamma_{LO,c}$	43	1	42	1	41	2	39.9	0.9	39	1	38	2

Table 4.1.1: Fitted Parameters Using the Factorized Model for the Dielectric Function When Fitting the Reflectance - TiO_2. Par = Parameter. Unc = Uncertainty.

	CD 5%							
Temp. (K)	4K	4K	100K	100K	200K	200K	300K	300K
	Par	Unc	Par	Unc	Par	Unc	Par	Unc
number of a oscillators	3		3		3		3	
number of c oscillators	1		1		1		1	
$\varepsilon_{\infty,a}$	5.46	0.01	5.43	0.01	5.27	0.01	5.305	0.008
$\varepsilon_{\infty,c}$	7.40	0.02	7.56	0.02	7.66	0.02	7.73	0.01
ω_{TO,a_1}	158.0	0.6	162.9	0.7	174.7	0.8	184.6	0.8
Γ_{TO,a_1}	10	1	10	1	22	1	28	1
ω_{LO,a_1}	830.4	0.8	828.6	0.9	834.3	0.8	837.8	0.7
Γ_{LO,a_1}	69.0	2	71	2	64	2	73	2
ω_{TO,a_2}	376.3	0.2	375.8	0.3	376.4	0.4	374.6	0.5
Γ_{TO,a_2}	12.2	0.4	15.2	0.6	25.7	0.8	31.0	0.9
ω_{LO,a_2}	352.8	0.3	352.9	0.3	349.0	0.4	348.8	0.3
Γ_{LO,a_2}	0.0	0.5	0.0	0.6	0.2	0.7	0.1	0.6
ω_{TO,a_3}	488.2	0.4	486.7	0.5	486.3	0.5	483.5	0.5
Γ_{TO,a_3}	44.4	0.7	45.1	0.8	55.4	0.8	61.8	0.8
ω_{LO,a_3}	420.9	0.3	421.2	0.4	420.1	0.4	418.4	0.4
Γ_{LO,a_3}	21.6	0.7	22.4	0.8	28.0	0.8	31.6	0.8
ω_{TO,a_4}								
Γ_{TO,a_4}								
ω_{LO,a_4}								
Γ_{LO,a_4}								
$\omega_{TO,c}$	140	2	144	2	163	2	174	1
$\Gamma_{TO,c}$	67	2	73	2	77	2	77	1
$\omega_{LO,c}$	787	1	789	1	792	1	794	1
$\Gamma_{LO,c}$	31	2	32	3	33	2	35	2

Table 4.1.2: Fitted Parameters Using the Factorized Model for the Dielectric Function When Fitting the Reflectance - CD 5%
Par = Parameter. Unc = Uncertainty.

	CD 10%							
Temp. (K)	4K	4K	100K	100K	200K	200K	300K	300K
	Par	Unc	Par	Unc	Par	Unc	Par	Unc
number of a oscillators	3		3		3		3	
number of c oscillators	1		1		1		1	
$\varepsilon_{\infty,a}$	6.51	0.02	6.57	0.02	6.51	0.02	5.637	0.009
$\varepsilon_{\infty,c}$	7.59	0.04	7.75	0.04	7.74	0.03	7.8	0.02
ω_{TO,a_1}	146	5	154	4	184	4	213	3
Γ_{TO,a_1}	147	6	145	7	140	8	143	9
ω_{LO,a_1}	828	1	828	1	833	1	836	1
Γ_{LO,a_1}	45	2	45	2	38	2	43	2
ω_{TO,a_2}	374.1	0.4	375.2	0.5	376.5	0.8	377	1
Γ_{TO,a_2}	13.5	0.8	18	1	24	2	28	2
ω_{LO,a_2}	348.3	1	344	1	342	2	343	2
Γ_{LO,a_2}	34.7	2	40	2	45	3	51	3
ω_{TO,a_3}	496.6	0.7	496.2	0.8	797	1	499	1
Γ_{TO,a_3}	59	1	64	1	75	2	85	2
ω_{LO,a_3}	405	1	405	1	404	1	400	2
Γ_{LO,a_3}	57	2	54	2	54	3	57	4
ω_{TO,a_4}								
Γ_{TO,a_4}								
ω_{LO,a_4}								
Γ_{LO,a_4}								
$\omega_{TO,c}$	158	1	166	1	176	1	180	1
$\Gamma_{TO,c}$	58	2	64	2	68	2	71	2
$\omega_{LO,c}$	791	2	791	2	792	2	792	2
$\Gamma_{LO,c}$	35	3	34	3	34	3	34	3

Table 4.1.3: Fitted Parameters Using the Factorized Model for the Dielectric Function When Fitting the Reflectance - CD 10%
Par = Parameter. Unc = Uncertainty.

Appropriateness of using the factorized model

For TiO_2 and 5% co-doped the reflectances fit by the factorized model are compared to the measurements and are shown graphically in figures 4.1.4 and 4.1.5. The fits are good for the TiO_2 and 5% co-doped samples. The factorized model is able to follow the small dip in the third resstrahlen band. At T=4K the factorized model does not perform

as well as at T=300K. For example, for TiO_2 the model slightly overestimates the falling right half of the first resstrahlen band and underestimates the small peak on the left part of the third resstrahlen band. For co-doped 10% TiO_2 the reflectances fit by the factorized model are compared to the measurements and are shown graphically in figure 4.1.6. The factorized model does not perform as well as for TiO_2 and 5% co-doped samples. For instance the model fails to describe the structure in the third resstrahlen band. In addition, the uncertainties (see Table 4.1.3) are high for the a1 and c oscillators at 200K. These problems suggest that a Kramers-Kronig analysis may be a better choice.

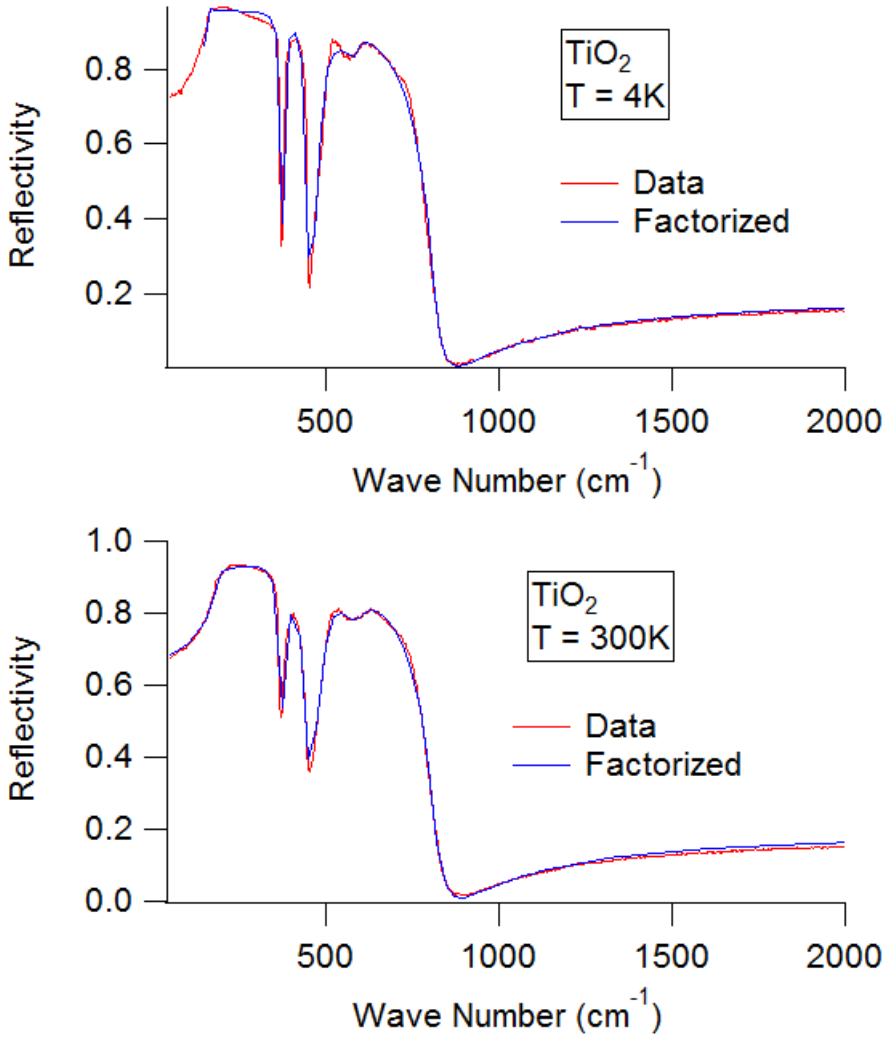

Figure 4.1.4: Comparison of TiO_2 Reflectance Data Against Calculated Values by the Factorized Model

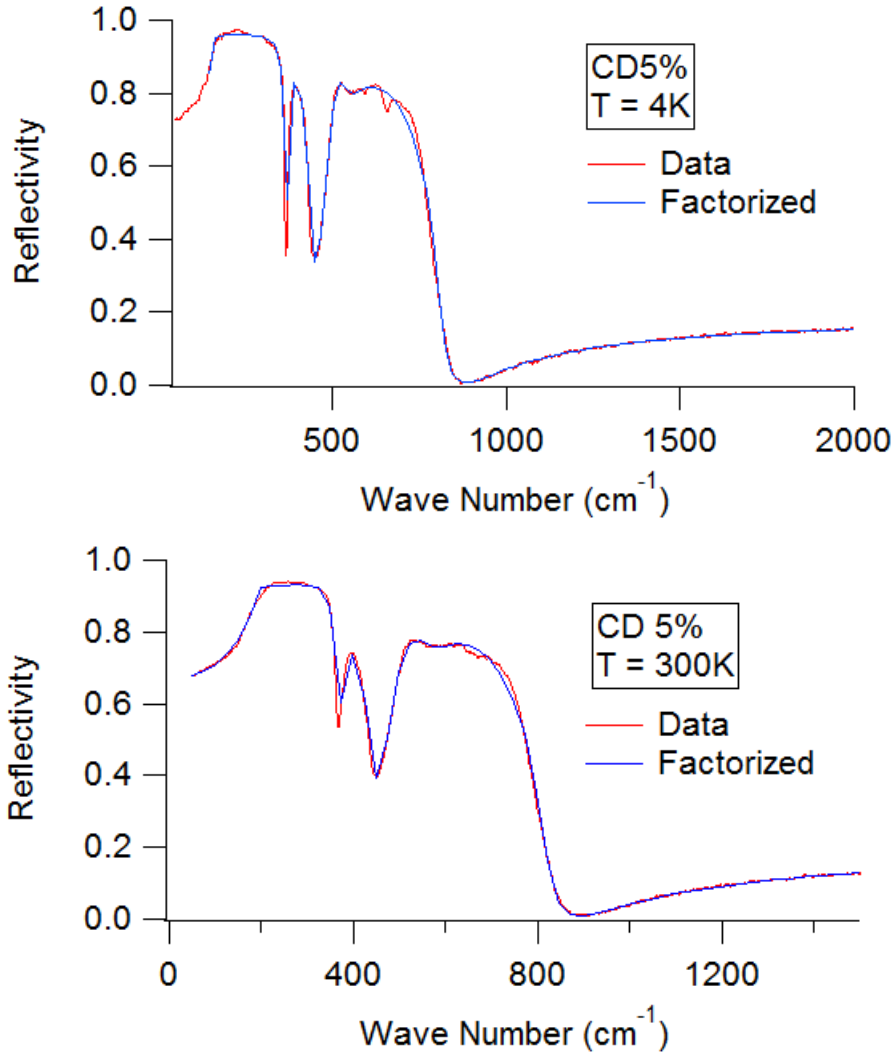

Figure 4.1.5: Comparison of Co-doped 5% TiO_2 Reflectance Data Against Calculated Values by the Factorized Model

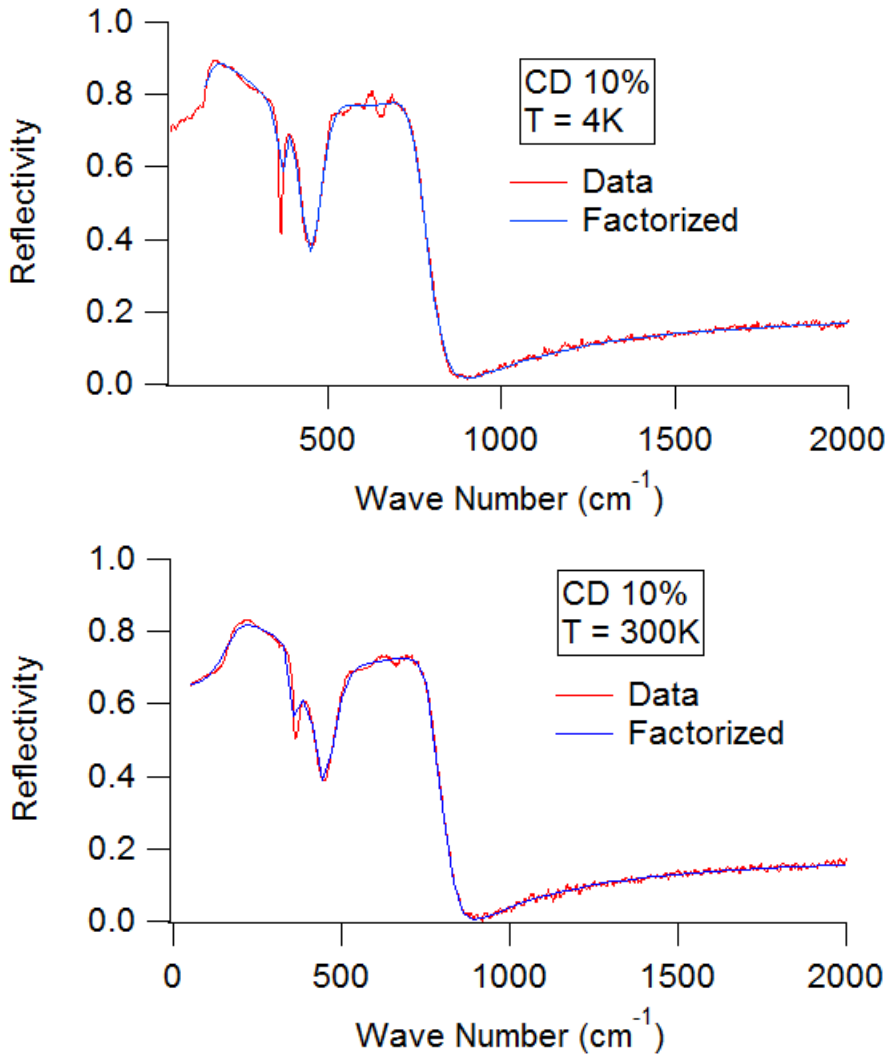

Figure 4.1.6: Comparison of Co-doped 10% TiO_2 Reflectance Data Against Calculated Values by the Factorized Model

4.2 Kramers-Kronig Analysis

The Kramers-Kronig analysis performs an integration over the interval $[0,\infty)$ (see section 2.4). The challenge is to construct an integrand that gives a reasonable description of reflectance data over the infinite interval. This can be done by constructing an "infinite" data set by (1) using data from various experimental data sets, (2) extrapolating values down to $\omega = 0$ from the data set with the lowest frequency, (3) interpolating reflectance values between disjoint data sets or approximating functions, and (4) extrapolating values to $\omega = \infty$.

Constructing the infinite interval of integration for Kramers-Kronig analysis

Data for the UV region was obtained from Cardona and Harbeke [94]. Cardona and Harbeke made polarized measurements parallel and perpendicular to the c axis. This work used a linear combination (eq. 4.2.1) of the Cardona and Harbeke data to obtain an approximation of reflectance from a ceramic.

$$R = \frac{2}{3}a_{axis} + \frac{1}{3}c_{axis} \tag{4.2.1}$$

Tanner [95] presents methods showing how the interpolations and extrapolations can be performed with an emphasis on a technique for extrapolating in the extreme UV to X-ray range. For instance, at low frequencies down to $\omega = 0$ the reflectance can be extrapolated using various models such as Drude or Lorentzian, a power-law function, or even a constant. In all cases the model is selected as appropriate for the sample material e.g. Drude model is appropriate for metallic samples. At the other end of the spectrum in the x-ray region $8.0 \times 10^4 - 2.4 \times 10^8$ cm^{-1} the reflectance of a material can be derived by using atomic scattering factors or functions (published tables in [96]) of the constituent elements. A scattering function $f(\omega)$ is a complex function of energy (frequency). $Re(f(\omega))$ has plateaus each of which is "...approximately equal to the number of "free" electrons at..." energy "ω". $Im(f(\omega))$ has "...peaks or discontinuities at absorption thresholds." The reflectance derivation assumes a material equals the linear combination of its atoms and, therefore, the complex dielectric function ε of the material (which depends on the absorption of energy and the separation of "free" charge) contains a term that equals a linear combination of the scattering functions of each element, where the weight of each function equals the number density of the constituent element (see Tanner [95] eq. 11). From ε one can use the Fresnel equations 2.4.11 and 2.4.12 to obtain the reflectance. The observed data set ends with the x-ray region data. The Kramers-Kronig integration must occur to ∞. The contribution to the phase is calculated analytically over this interval by assuming the free electron form ω^{-4} (Homes [97]). In the experiments where the region of highest frequency data do not reach the x-ray region, the reflectance is approximated by a "bridge" (interpolating) function that connects the two regions. Tanner [95] presents results that show the conductivity derived from a Kramers-Kronig analysis appears to be insensitive to the form of the bridge function.

Several data sets were connected to the data from this work to construct the infinite interval for the numerical integration used to perform the KK analysis on undoped TiO_2 (Table 4.2.1). These data sets are shown graphically in figures 4.2.1, 4.2.2, and 4.2.3. This work uses the factorized model to extrapolate low frequency data down to $\omega = 0$.

Data set	Range (cm^{-1})	Source	Reference
extrapolation	$1-50$	this work; calculated values using fitted parameters for factorized model. data set: rlow_tio2_300	Tables 4.1.1, 4.1.2, 4.1.3
experiment	$50-8000$	this work. data set: R_tio2_1300_100_300k_wr	
experiment	$8000-100000$	Cardona and Harbeke (1965). data set: R_tio2_vis_uv_average	[94]
bridge	$100000-2\times10^5$	bridge made using Drude-Lorentz model data set: r_link_UV_henke	
extrapolation	$2\times10^5-2.4\times10^8$	Tanner using modified Henke atomic scattering functions data set: R_henke_tio2_scaled	[95]
extrapolation	$2.4\times10^8-\infty$	approximation $=\omega^{-4}$	[95]

Table 4.2.1: Data Sets Used in Kramers-Kronig Analysis on TiO_2 at 300K

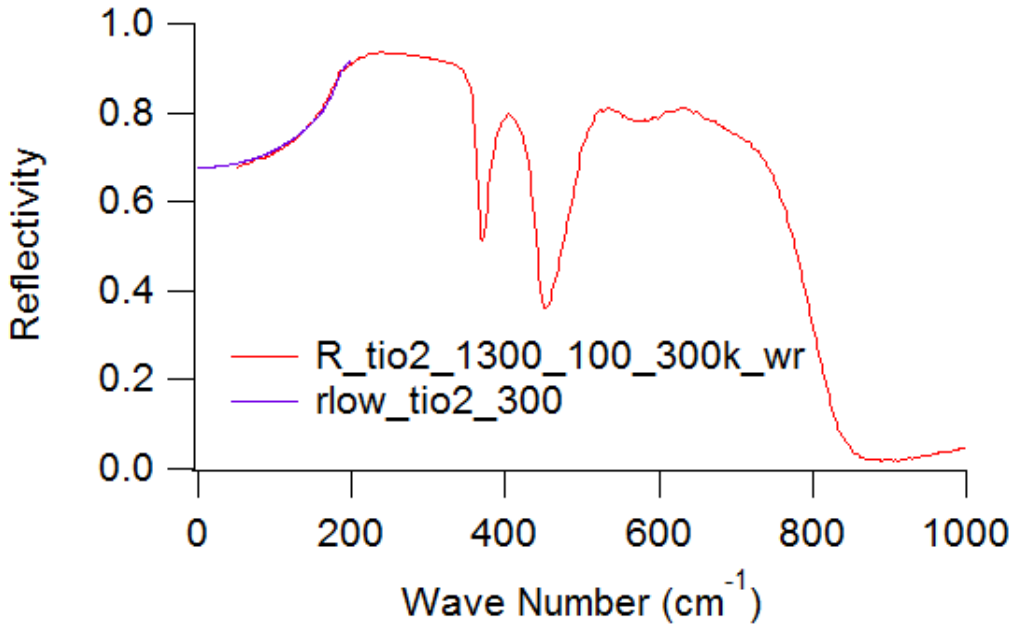

Figure 4.2.1: Reflectivity Data for TiO_2 in Range 0-1000 cm^{-1}.

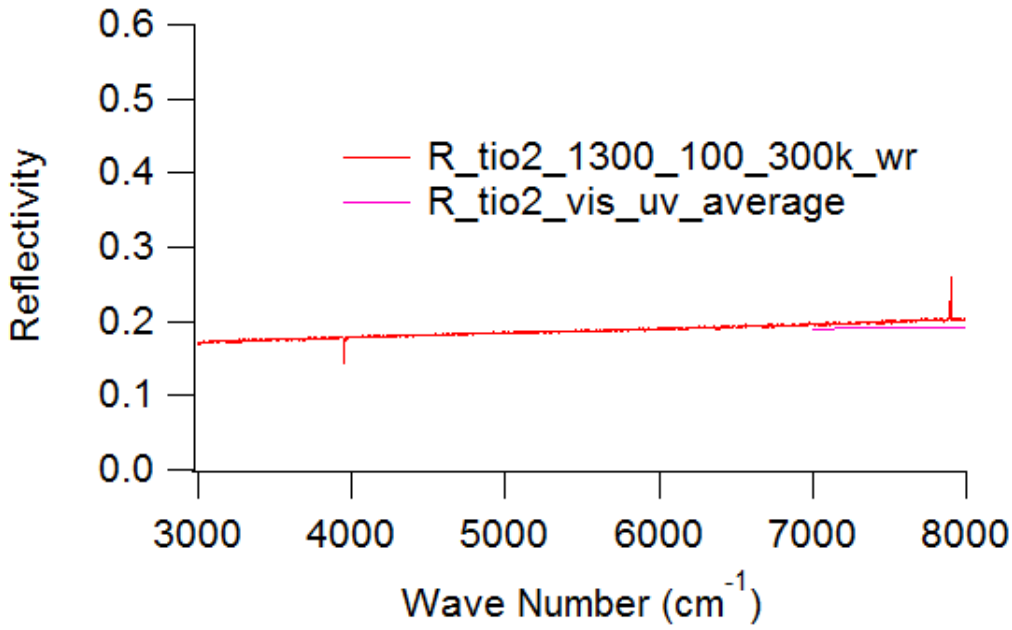

Figure 4.2.2: Reflectivity Data for TiO_2 in Range 3000-10000 cm^{-1}. The data labelled R_tio2_vis_uv_average is the average of the data from Cardona [94].

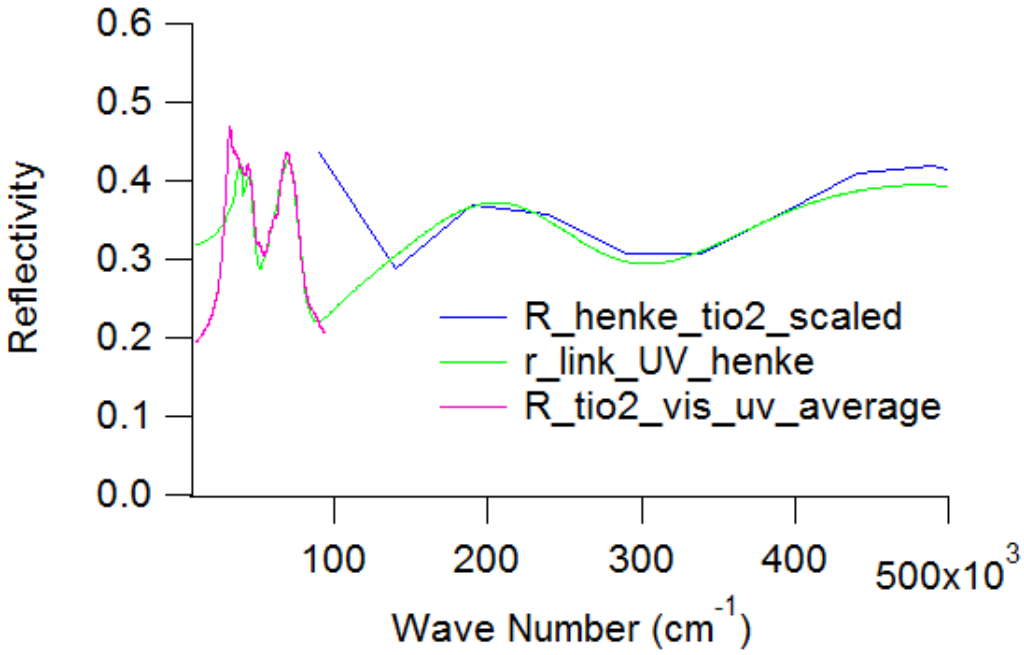

Figure 4.2.3: Reflectivity Data for TiO_2 in Range 10000-500000 cm^{-1}. The data labelled R_tio2_vis_uv_average is the average of the data from Cardona [94].

Kramers-Kronig Real Conductivity

The results of the KK analysis on optical conductivities are shown graphically in figures 4.2.4 and 4.2.5. There are only three modes visible because the c-mode parameters are quite similar to a1 and they overlap. The mode that softens occurs between 150 and 200 cm^{-1} at temperatures between 4 and 300K. The peak of the mode that softens becomes markedly higher as temperature decreases. The peak of the mode that softens is much higher than the other two modes which are roughly the same height. In general, all modes become narrower as temperature decreases reflecting a decrease in Γ or the scattering parameter. There appear to be to be four impurity modes that increase in oscillator strength with co-doping level centered near $\omega \approx$ 136, 447, 654 and 793 cm^{-1}. It is interesting to note that four Raman active modes were previously observed in Rutile [98] at $\omega \approx$ 143, 447, 612 and 826 cm^{-1}. It is possible that the co-doping process breaks lattice symmetry which causes the Raman active modes to develop a dipole moment and become weakly IR active.

Figures 4.3.1, 4.3.2 and 4.3.3 emphasize the mode that softens. At 4 and 300K (see figure 4.3.3) the peaks of the 10% co-doped sample are noticeably asymmetric - more sharply increasing on the left side of the peak and more gently decreasing on the right side. These peaks are also broader than those for undoped and 5% co-doped samples indicating an increase in scattering rate. An additional structure is visible ~130 cm^{-1} in the co-doped

samples, but not the undoped sample. This feature is not temperature dependent and is not a soft mode.

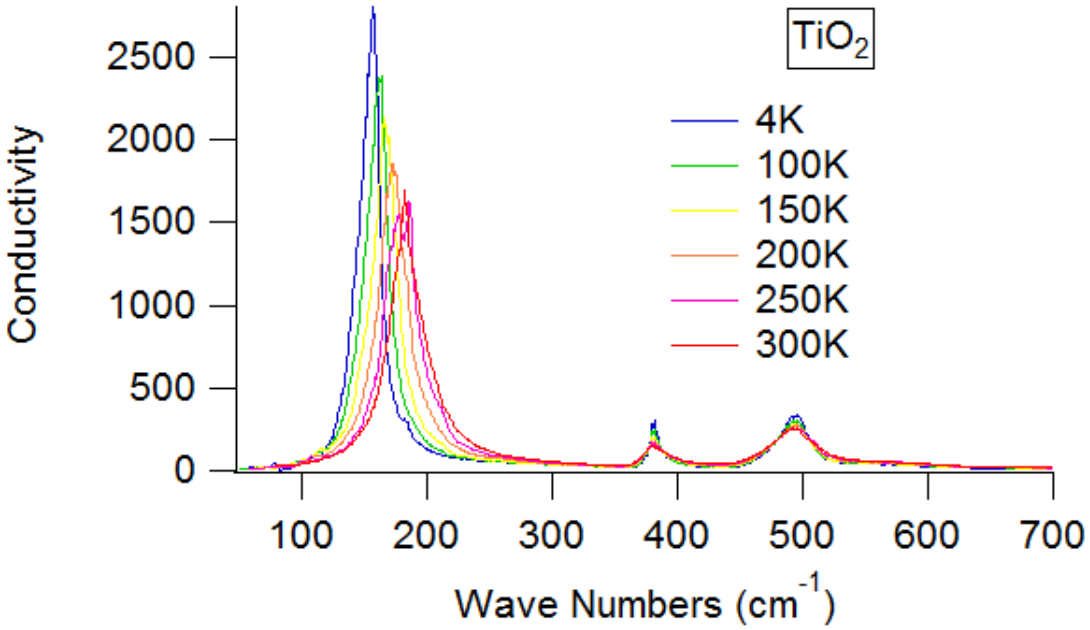

Figure 4.2.4: KK Real Conductivity versus Temperature for Un-Doped TiO_2

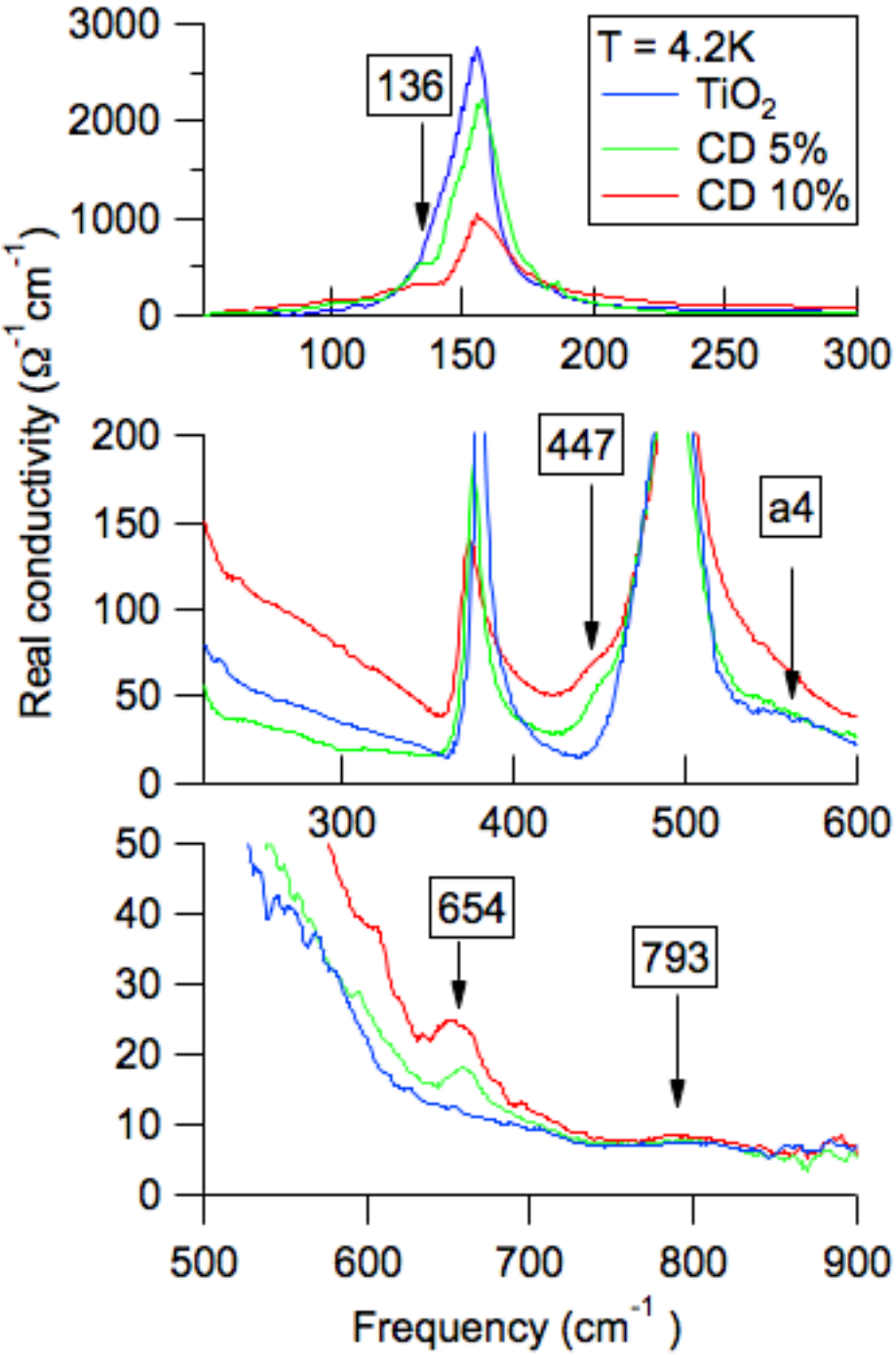

Figure 4.2.5: Real Conductivity for TiO_2, co-doped 5%, co-doped 10% at 4K

Permittivity

The results of the KK analysis on permittivity at 4 and 300 K are shown in figure 4.2.6. Similar results occur for temperatures between 4 and 300 K. Note that co-doping actually

decreases the permittivity for frequencies below the mode that softens.

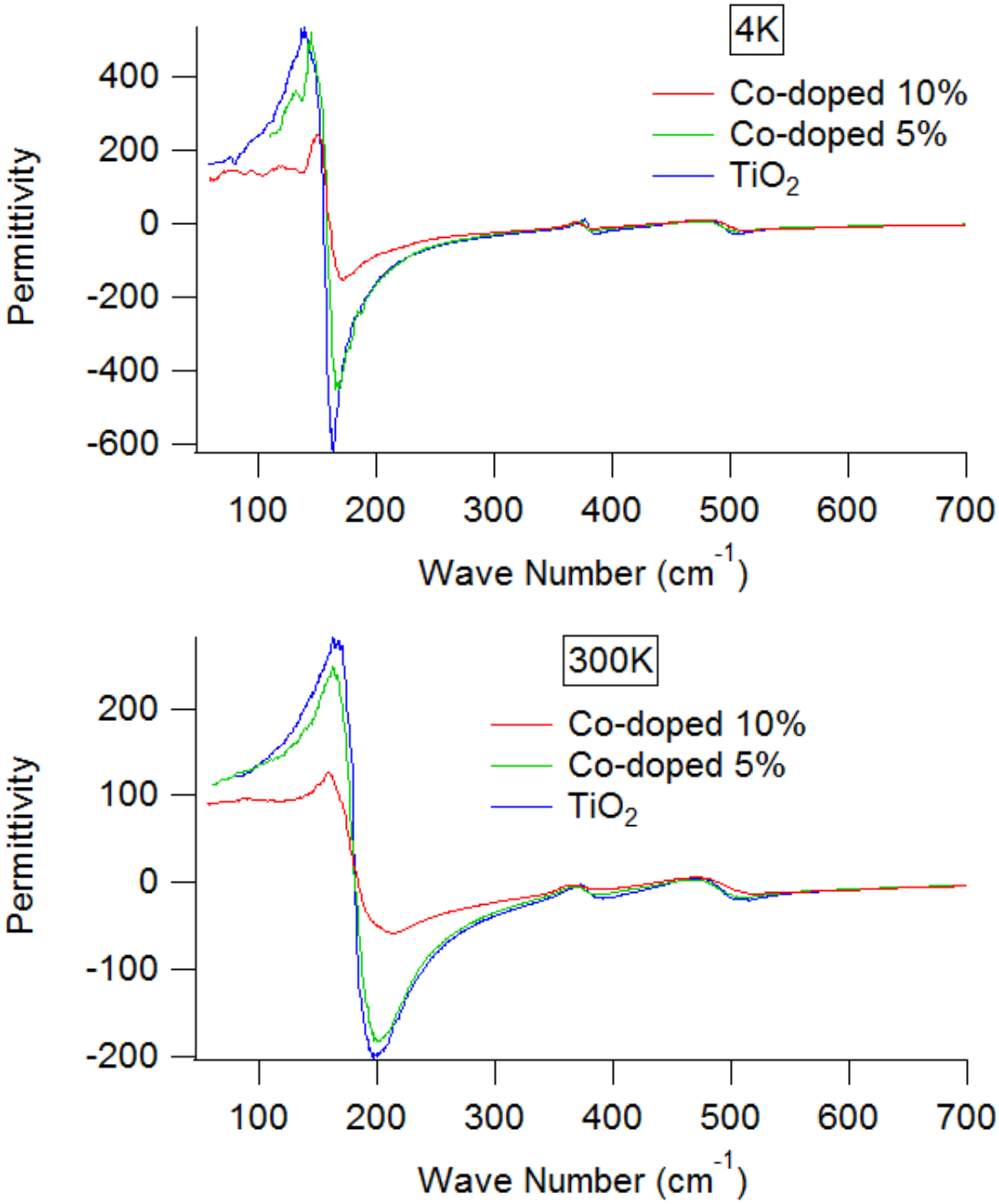

Figure 4.2.6: Comparison of Permittivity using Kramers-Kronig Analysis

4.3 Effect of Doping on the Mode that Softens

As temperature increases (or decreases) monotonically a lattice may undergo a change in structure. A soft phonon is a phonon which shows a decrease in frequency as the tran-

sition temperature is approached [99, 100]. In particular, $(\omega^2) \propto T - T_c$ [101] where T_c is the critical temperature at which the transition occurs. The Lyddane-Sachs-Teller equation [76]

$$\frac{\omega_L^2}{\omega_T^2} = \frac{\varepsilon(0)}{\varepsilon(\infty)}$$

implies that as $\omega_T \to 0$, $\varepsilon(0) \to \infty$. The Fresnel equations 2.4.11 and 2.4.12 relate the reflectance R and the dielectric function ε. As $\varepsilon(0) \to \infty$, $R(0) \to 1$. Putting all these relations together gives that as the temperature approaches the critical temperature, the reflectance at $\omega = 0$ approaches 1. Soft phonons are associated with phase transitions or changes in crystal structure and are important to the study of ferroelectric structure (for examples see [100, 102–107]).

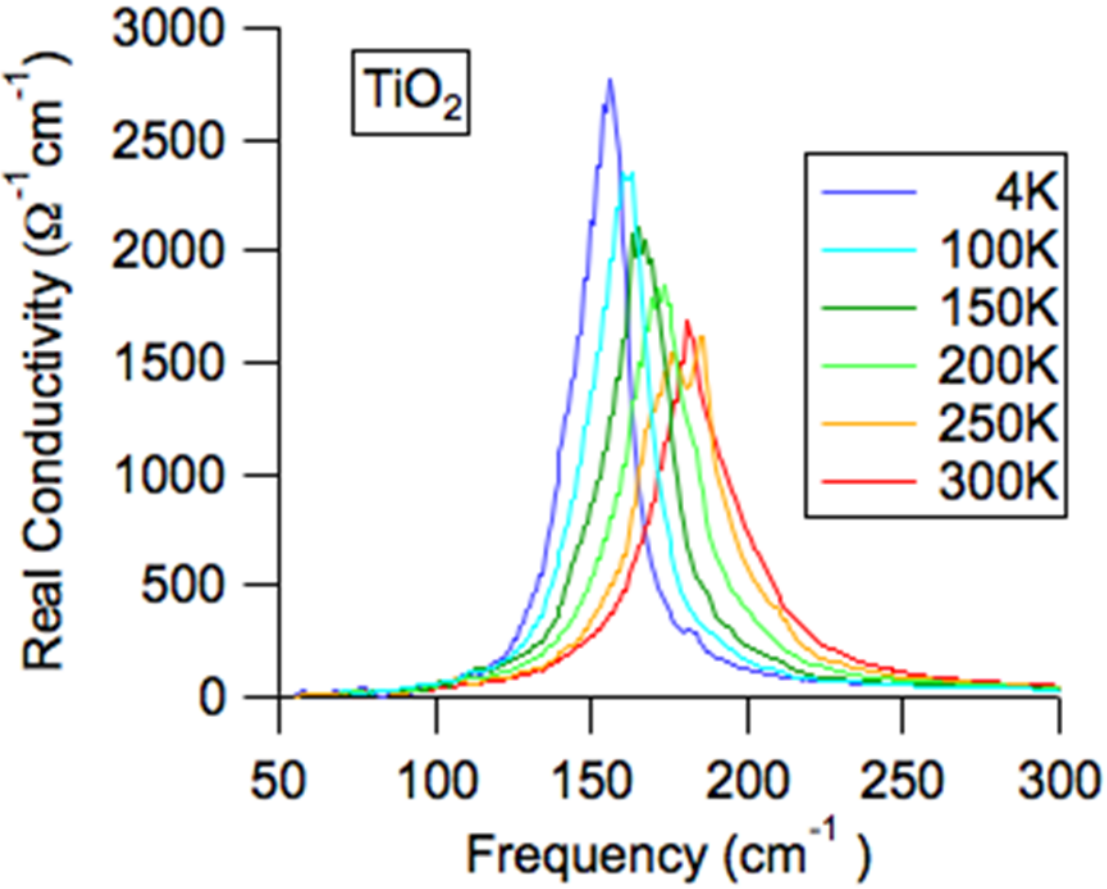

Figure 4.3.1: The KK real conductivity of TiO_2 4K-300K measurements.

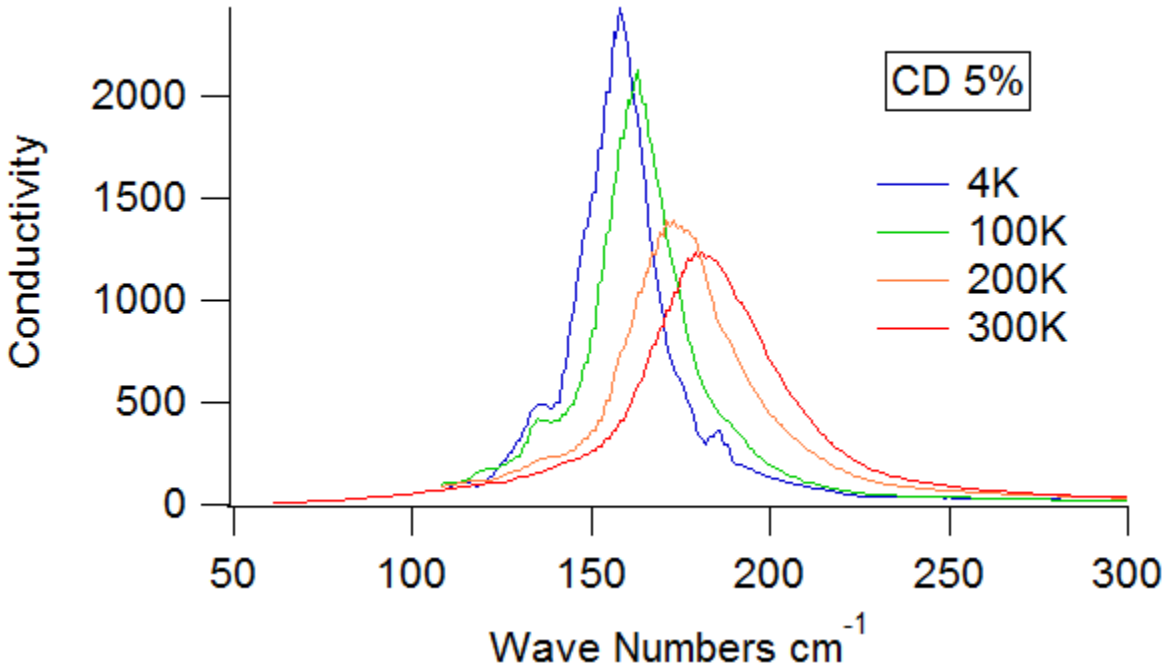

Figure 4.3.2: The KK real conductivity of CD 5% 4K-300K measurements.

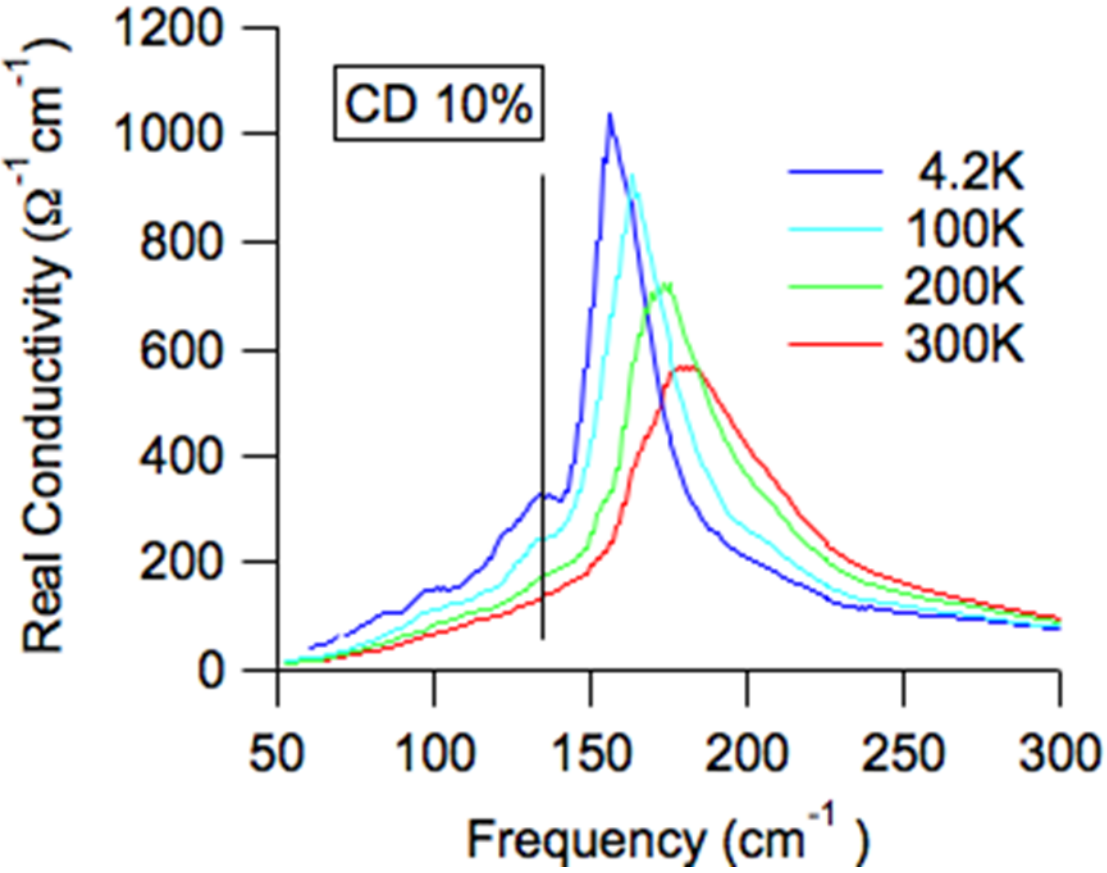

Figure 4.3.3: A new mode appears at ~130cm^{-1} most noticably in the 4.2K measurement.

The 5% and 10% figures show the mode as discussed above appearing at ~136 cm^{-1} in the 200K, 100K, and 4K measurements. The frequency of this impurity induced mode is temperature independent and therefore is not soft.

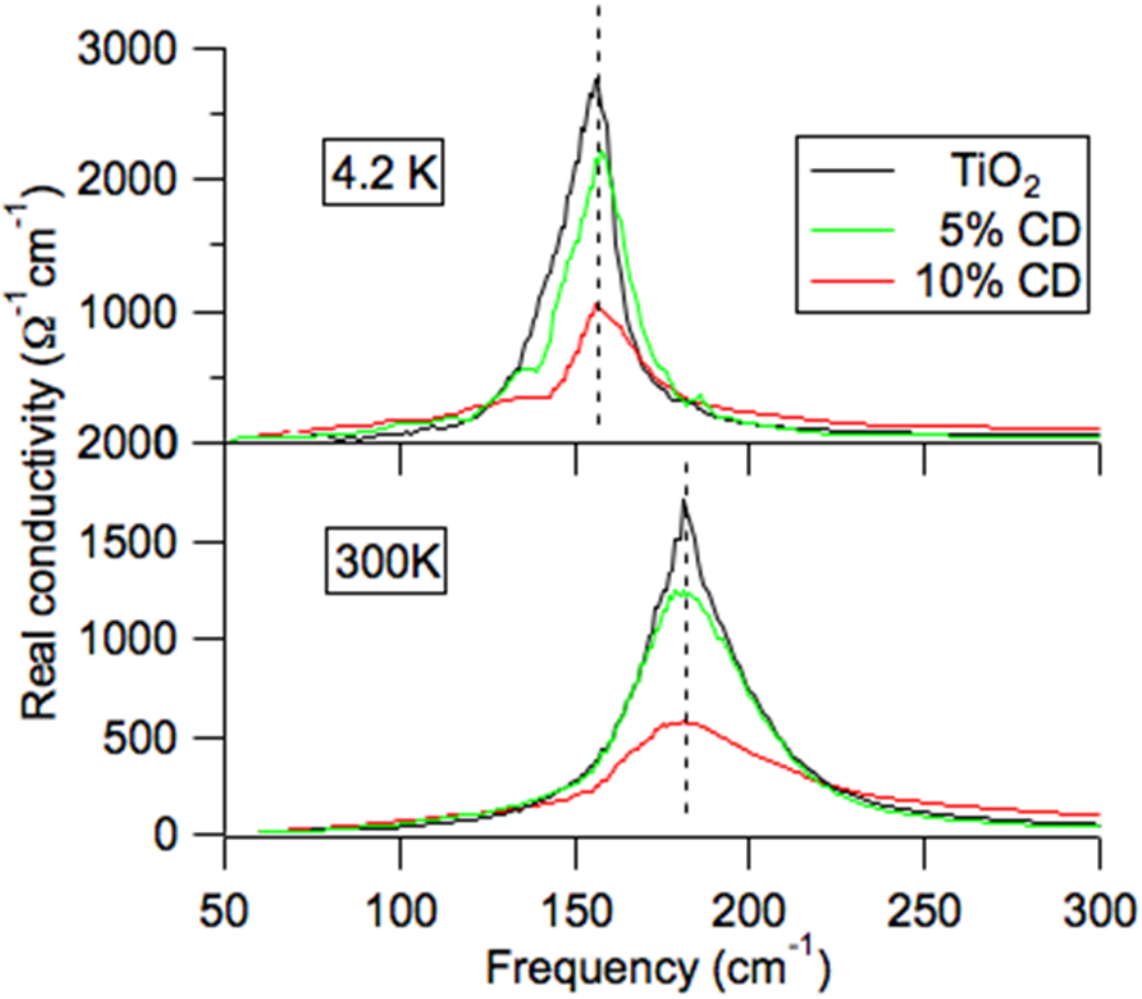

Figure 4.3.4: Comparison of the softening-mode real conductivity in all three doping levels at 4K and 300K.

Figure 4.3.4 shows the decrease of the softening-mode frequency between 300K and 4.2K in all three doping levels. From this it can be seen ω_{TO} is almost independent of doping level. However, the height of the peak is decreased by increased doping level. In all cases the height decreases at higher temperature and the order of the peaks is preserved. At the 10% level there is a widening of the peak and a lowering of the height. This is expected because the electrons are interacting with a higher amount of impurities and lattice defects. The TiO_2 peak is higher than the CD 5% peak, which is higher than the CD 10% peak. Co-doping decreases the real conductivity. Co-doping at 10% reduces the real conductivity disproportionately more than co-doping at 5%. This may be due to the co-doping causing defects in the basic TiO_2 lattice and localizing hopping electrons [1] which will tend to reduce the real conductivity.

The spectral weight for the mode that softens was calculated via eq. 4.3.1 where the real conductivity outside the interval [75, 350] is presumed to be 0 and does not affect the value of the integral. The peak for all temperatures remains inside this frequency region and the same interval of integration may be used.

$$W = \int_{75}^{350} \sigma_1(\omega) d\omega \tag{4.3.1}$$

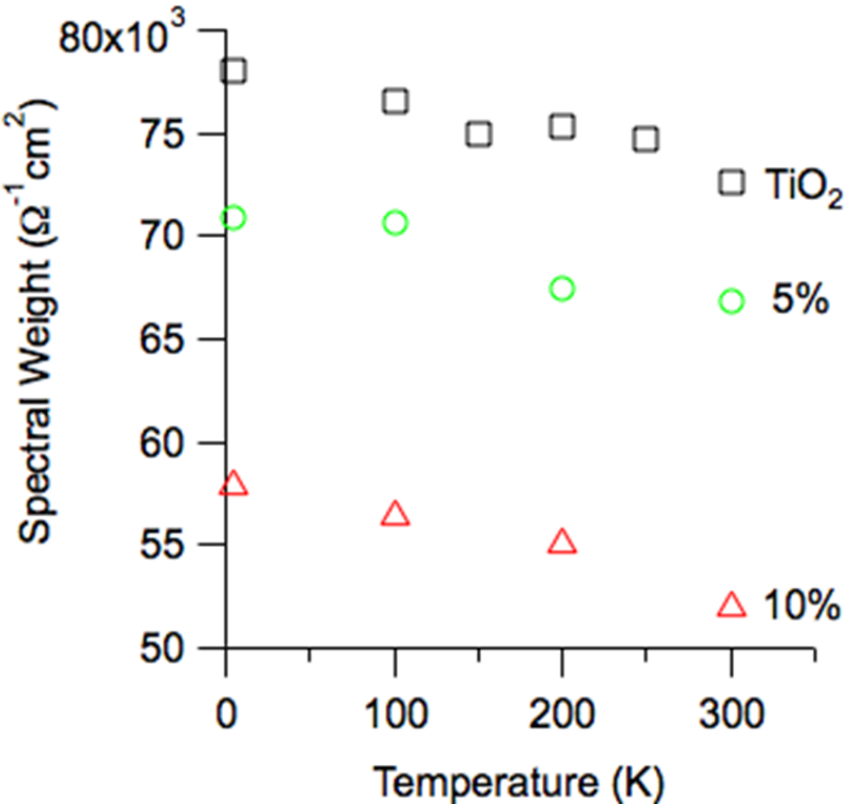

Figure 4.3.5: Comparison of spectral weights among all doping levels as related to temperature. Spectral weights calculated by integrating from 75 to 350 cm^{-1}.

Fig. 4.3.5 shows the results of calculating the spectral weight for TiO_2, CD 5%, and CD 10% at 4, 100, 200, and 300K.

Recall eq. 4.3.1 for the spectral weight. In general

$$W = \int_{-\infty}^{\infty} \sigma_1(\omega) d\omega \tag{4.3.2}$$

The sum rule for conductivity gives that

$$\int_0^\infty \sigma_1(\omega) d\omega = \frac{\pi e^2 n}{2m} \tag{4.3.3}$$

where e is the charge of an electron, m is the (normal) mass of an electron, and n is the number of electrons (see [76]). Therefore, the spectral weights calculated by eq. 4.3.1 are approximations of $\pi e^2 n$. The decrease in spectral weight is difficult to understand but may be due to differences in porosity in the sample as will be discussed below. TiO_2 is less dense than CD 5% so the decrease in spectral weight may be a real effect. The CD 10% is less dense than the CD 5% so this effect could be due to a combination of porosity and doping.

Lichtenecker Adjustment to the Factorized Model

Table 4.3.1 shows that the ceramic pellets studied were somewhat porous. This means the effective dielectric function of the pellet comes not only from co-doped grains of TiO_2, but also from "grains" of air. The Lichtenecker model [108, 109] gives a way to calculate an effective dielectric function for porous ceramics comprised of multiple media. The ceramic pellets in this work are modelled as formed by "grains" (a) with c-axis perpendicular to polarized light, (b) with c-axis parallel to polarized light, and (c) of air.

Sample	IR
TiO_2	1300°C
	$p = 0.16 \pm 0.02$
CD 5%	1450°C
	$p = 0.17 \pm 0.02$
CD 10%	1450°C
	$p = 0.24 \pm 0.02$

Table 4.3.1: Sintering Temperatures and Porosity. The porosity was estimated from the pellet mass and geometry and by comparing the measured and theoretical mass densities.

For a non-porous ceramic pellet the Lichtenecker model gives the dielectric function as

$$\varepsilon^\alpha_{effective} = \frac{2}{3}\varepsilon^\alpha_a + \frac{1}{3}\varepsilon^\alpha_c \tag{4.3.4}$$

The superscript α is an exponent that serves as a fitting parameter. α is related to the topology of the grains and whether or not the phase is percolated [109]. The coefficients $\frac{2}{3}$ and $\frac{1}{3}$ are weights given to the two modes because there are two directions perpendicular to the c-axis (the a mode) and only one direction parallel to the c-axis (c-mode). The dielectric functions ε_a and ε_c are modelled by the factorized model equation 4.1.1 [108].

For a porous ceramic pellet the "air grains" are added as

$$\varepsilon^{\alpha}_{effective} = \left(\frac{2}{3}\varepsilon^{\alpha}_{a} + \frac{1}{3}\varepsilon^{\alpha}_{c}\right)(1-p) + p\varepsilon^{\alpha}_{air}$$

$$\varepsilon^{\alpha}_{effective} = \frac{2}{3}(1-p)\,\varepsilon^{\alpha}_{a} + \frac{1}{3}(1-p)\,\varepsilon^{\alpha}_{c} + p\varepsilon^{\alpha}_{air} \tag{4.3.5}$$

where p is the porosity. Equation 4.3.5 reduces to the equations for a non-porous ceramic when $p = 0$ (no air pores) and a sample of all air when $p = 1$ (no ceramic grains). Consider ε_a. Equation 4.3.5 shows that the contribution of ε_a to the overall ε is reduced by a factor $1-p$. This has the effect of making the "a" oscillators' strength appear to be weakened. Similarly the "c" oscillator strength appears to be weakened. Overall, equation 4.3.5 shows that as porosity increases the effective dielectric function tends toward that of air ($\varepsilon_{air} \approx 1$). Fig. 4.3.6 shows the effect of porosity on ε_1 for a range of values of p that include values shown in table 4.3.1. Nuzhnyy et al. [108] show detailed graphs (their fig. 5) of the effect of porosity and α on $\varepsilon_1\,(=\mathrm{Re}\,(\varepsilon))$ for $\mathrm{Pb}\left(\mathrm{Mg}_{\frac{1}{3}}\mathrm{Nb}_{\frac{2}{3}}\right)\mathrm{O}_3$. Conductivity and reflectance and can be determined from the dielectric function ε. Therefore, the effects of porosity on conductivity and reflectance can be deduced from the dielectric function. These effects are shown in figs. 4.3.7 and 4.3.8.

Assuming $\alpha = 1$ equation 4.3.5 becomes

$$\varepsilon_{eff} = \frac{2}{3}(1-p)\,\varepsilon_a + \frac{1}{3}(1-p)\,\varepsilon_c + p\varepsilon_{air} \tag{4.3.6}$$

Consider

$$\begin{aligned}
\frac{\partial}{\partial p}\varepsilon_{eff} &= \frac{\partial}{\partial p}\left[\frac{2}{3}(1-p)\,\varepsilon_a + \frac{1}{3}(1-p)\,\varepsilon_c + p\varepsilon_{air}\right] \\
&= -\frac{2}{3}\varepsilon_a - \frac{1}{3}\varepsilon_c + \varepsilon_{air} \\
&= \varepsilon_{air} - \left(\frac{2}{3}\varepsilon_a + \frac{1}{3}\varepsilon_c\right) \\
&= \varepsilon_{air} - \varepsilon_{non-porous}
\end{aligned}$$

This shows that if $Re\left\{\varepsilon_{non-porous} > \varepsilon_{air}\right\}$, then $Re\left\{\varepsilon_{eff}\right\}$ is decreasing and if $Re\left\{\varepsilon_{non-porous} < \varepsilon_{air}\right\}$, then $Re\left\{\varepsilon_{eff}\right\}$ is increasing. The second partial derivative with respect to p is 0; therefore,

the rate of decrease (or increase) is constant. At $\varepsilon_{non-porous} = \varepsilon_{air}$, ε_{eff} is non-changing with respect to porosity. These equations mean that the effect of changing p at $\alpha = 1$ is as follows. For $\varepsilon_1 < 1$ as p increases, ε_1 decreases linearly in p. For $\varepsilon_1 > 1$ as p increases, ε_1 increases linearly in p. In other words,ε_1 tends to get closer to the real axis $\varepsilon_1 = 0$ as p increases. Fig. 4.3.6 graphically shows this effect for a hypothetical single oscillator using the factorized model. Similar statements can be made for the imaginary part of ε_{eff}.

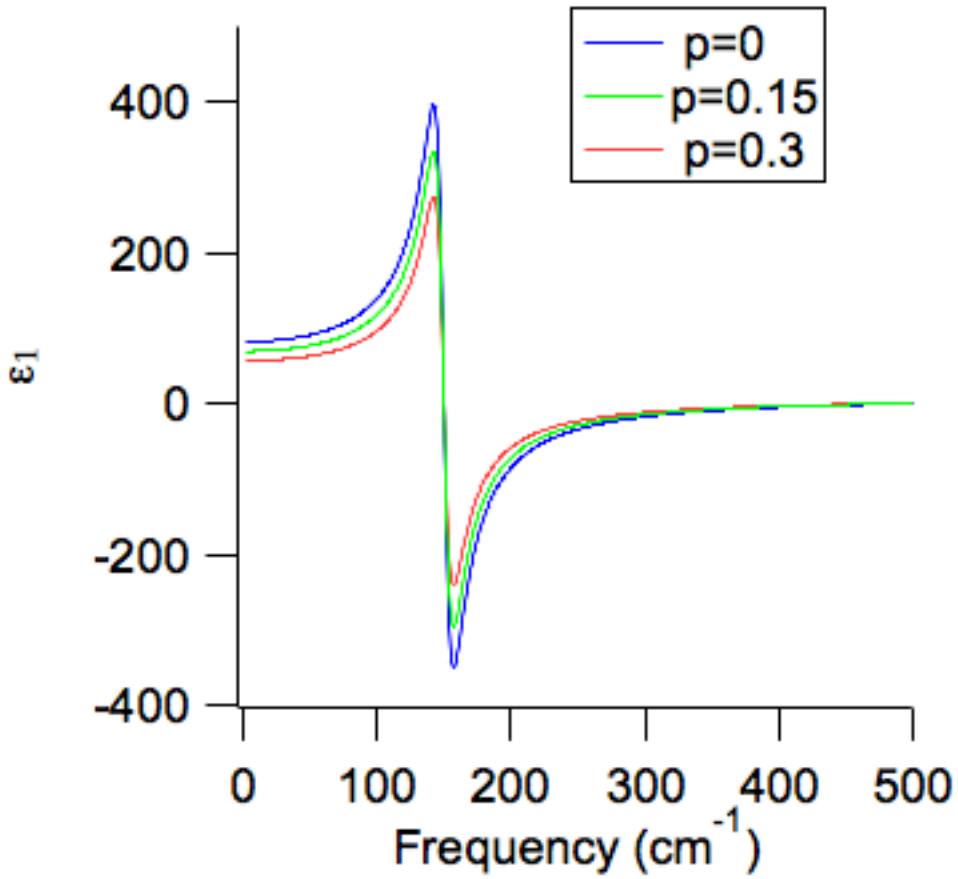

Figure 4.3.6: Effect of porosity on ε_1, assumes factorized model for both ε_a and ε_c. In the "a" direction there is one oscillator: $\omega_{TO} = 150\ \text{cm}^{-1}$, $\Gamma_{TO} = 15\ \text{cm}^{-1}$, $\omega_{LO} = 5000\ \text{cm}^{-1}$, $\Gamma_{LO} = 15\ \text{cm}^{-1}$, $\varepsilon_\infty = 6.843$. In the "c" direction there is one oscillator: $\omega_{TO} = 150\ \text{cm}^{-1}$, $\Gamma_{TO} = 15\ \text{cm}^{-1}$, $\omega_{LO} = 5000\ \text{cm}^{-1}$, $\Gamma_{LO} = 15\ \text{cm}^{-1}$, $\varepsilon_\infty = 8.427$.

The real conductivity is given by

$$\sigma_1(\omega) = \varepsilon_0 \omega \varepsilon_2(\omega)$$

For a porous ceramic

$$\begin{aligned}
\sigma_{eff,1}(\omega) &= \varepsilon_0 \omega \varepsilon_{eff,2}(\omega) \\
&= \varepsilon_0 \omega \left[\frac{2}{3}(1-p)\varepsilon_{a,2} + \frac{1}{3}(1-p)\varepsilon_{c,2} + p\varepsilon_{air,2} \right] \\
&= \varepsilon_0 \omega \left[\frac{2}{3}(1-p)\varepsilon_{a,2} + \frac{1}{3}(1-p)\varepsilon_{c,2} + p \cdot 0 \right] \\
&= \varepsilon_0 \omega \left[\frac{2}{3}(1-p)\varepsilon_{a,2} + \frac{1}{3}(1-p)\varepsilon_{c,2} \right] \\
&= (1-p)\varepsilon_0 \omega \left[\frac{2}{3}\varepsilon_{a,2} + \frac{1}{3}\varepsilon_{c,2} \right] \\
&= (1-p)\varepsilon_0 \omega \varepsilon_{non-porous-ceramic,2}(\omega)
\end{aligned}$$

which finally gives

$$\sigma_{eff,1}(\omega) = (1-p)\sigma_{non-porous-ceramic,1}(\omega) \tag{4.3.7}$$

Equation 4.3.7 shows that effective conductivity decreases linearly as porosity increases. Fig. 4.3.7 illustrates this effect for a hypothetical single oscillator using the factorized model (as before).

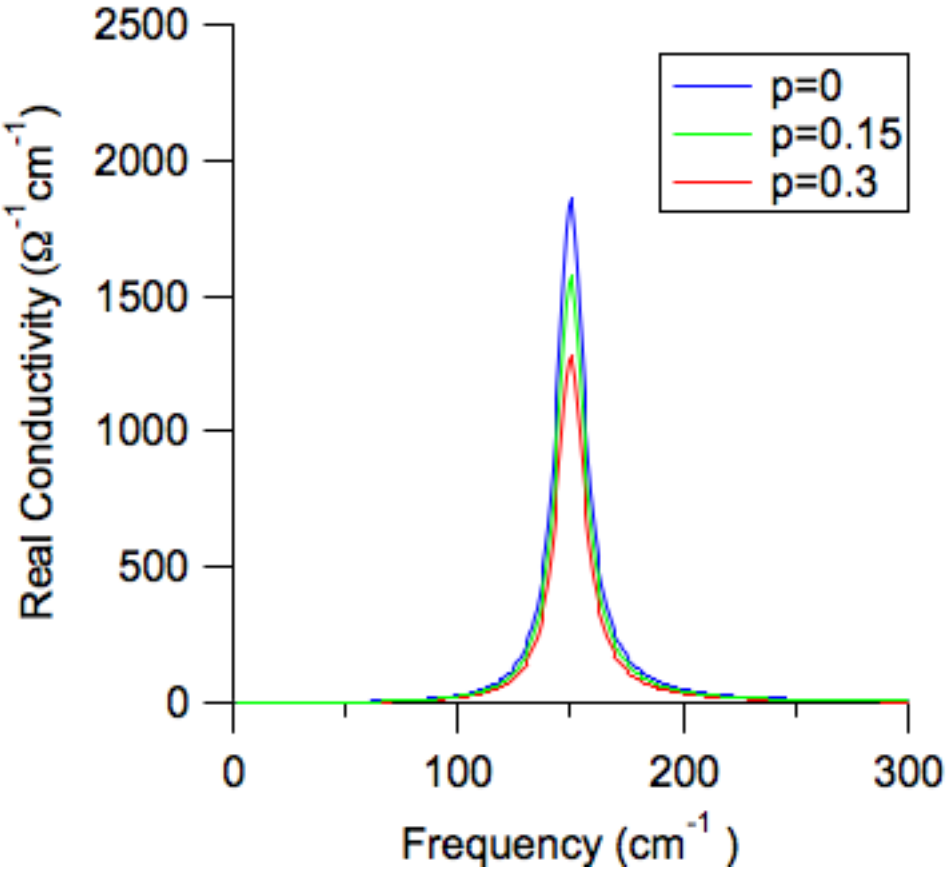

Figure 4.3.7: Effect of porosity on σ_1. Same model as used in fig. 4.3.6.

Apply the definition of spectral weight, equation 4.3.2, to equation 4.3.7 to get the spectral weight of a porous ceramic in terms of a non-porous ceramic.

$$\int_{-\infty}^{\infty} \sigma_{eff,1}(\omega)d\omega \quad = \quad (1-p)\int_{-\infty}^{\infty} \sigma_{non-porous-ceramic,1}(\omega)\,d\omega$$

Let $W(p)$ denote the spectral weight of a ceramic with porosity p. The above equation becomes

$$W(p) = (1-p)\,W(0) \tag{4.3.8}$$

Taking the partial derivative of W with respect to p gives

$$\frac{\partial W}{\partial p} = -W(0)$$

which shows that the spectral weight of a porous ceramic is decreasing at a constant rate as a function of porosity.

The reflectance R approaches 0 as porosity approaches 1. Fig. 4.3.8 illustrates this effect for a hypothetical single oscillator using the factorized model. The difference in spectral weight between 5% and 10% co-doped samples (fig. 4.3.5) could be due to a difference in porosity. More work needs to be done to investigate this observation.

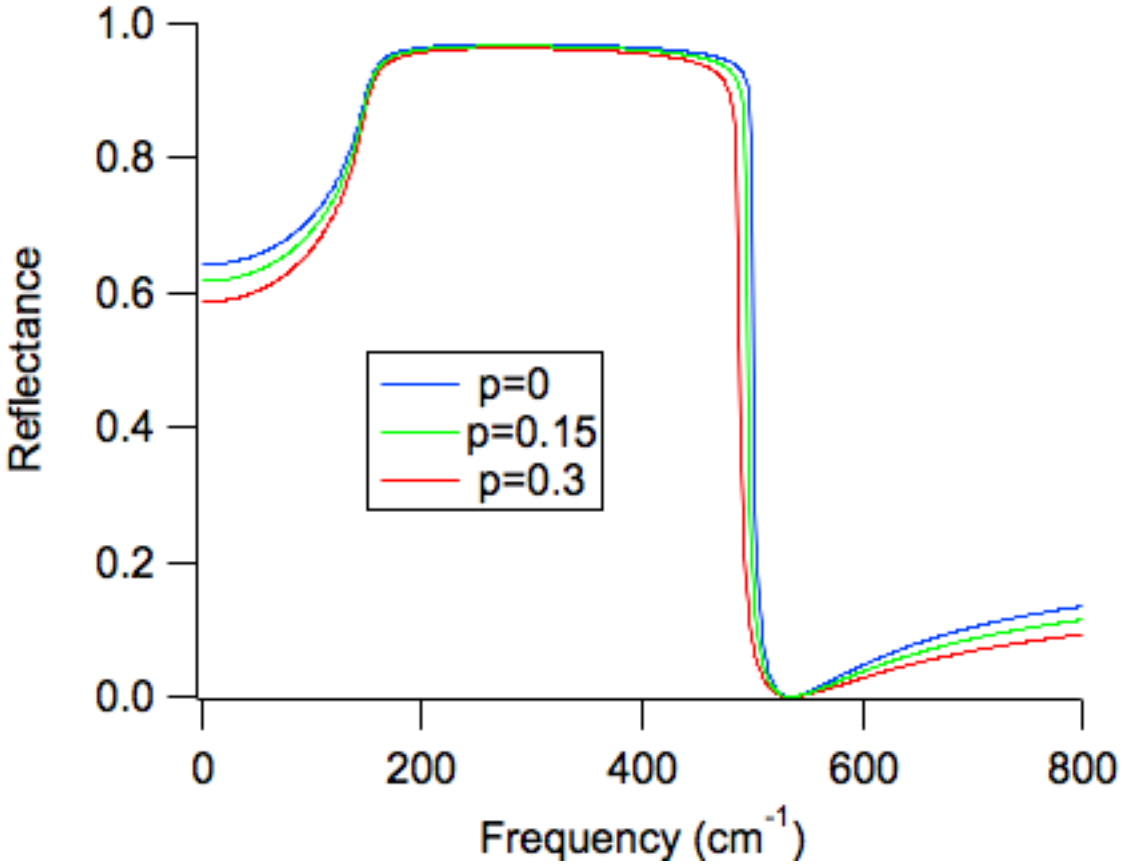

Figure 4.3.8: Effect of porosity on reflectance. Same model as used in fig. 4.3.6.

Chapter 5

Conclusions

This thesis work studied rutile TiO_2 co-doped with In (electron acceptor) and Nb (electron donor) at 5% and 10% to explore the effect of co-doping on the infrared active (IR) modes and the complex dielectric response function between 50 and 8000 cm^{-1} (1.5 - 240 THz).

Co-doping rutile appears to decrease the permittivity at frequencies just below the mode that softens. It appears that the increase in permittivity recently observed elsewhere [1] is not caused by doping induced changes to the phonon modes. The overall effect of co-doping is to make the sample less reflective and this effect is strongest in the region surrounding the second band. In 10% co-doped rutile this region looks like a dip in the spectrum. For all levels of co-doping the first band is a mode that softens. The amount of doping does not affect the frequency of the mode that softens. The second and third bands do not shift significantly with decreasing temperature and, therefore, are hard modes.

Co-doping appears to introduce four new, impurity, phonon modes (seen in fig. 4.2.5) that increase in oscillator strength with increasing co-doping level. These modes are centered near $\omega \approx 136$, 447, 654 and 793 cm^{-1}. It is interesting to note that these IR active modes are close to four Raman active modes previously observed in rutile at $\omega \approx 143$, 447, 612 and 826 cm^{-1}. It is possible that the co-doping process causes the Raman modes to develop a dipole moment and become weakly IR active.

The spectral weight decreases with increasing co-doping. The decrease in spectral weight may be due to an increase in porosity which may be due to the increase in co-doping. The Lichtenecker model implies that ε_1 and σ_1 will decrease as porosity increases. Therefore, it is possible that the decrease of ε_1 and σ_1 for frequencies below the mode that softens is due to an increase in porosity resulting from the co-doping.

Bibliography

[1] Wanbiao Hu, Yun Liu, Ray L, Withers, Terry J. Frankcombe, Lasse Noren, Amanda Snashall, Melanie Kitchin, Paul Smith, Bill Gong, Hua Chen, Jason Schiemer, Frank Brink, and Jennifer Wong-Leung. Electron-pinned defect-dipoles for high-performance colossal permittivity materials. *Nature Materials*, 12:821–826, June 2013. doi: 10.1038/nmat3691.

[2] Anonymous. Dielectric constants of various materials, 2014. URL `http://www.deltacnt.com/99-00032.htm`. [Online; accessed 08-April-2014].

[3] Anonymous. Dielectric constant values, 2014. URL `http://www.clippercontrols.com/pages/Dielectric-Constant-Values.html`. [Online; accessed 08-April-2014].

[4] M.A. Subramanian, D. Li, N. Duan, B.A. Reisner, and A.W. Sleight. High Dielectric Constant in $ACu_3Ti_4O_{12}$ and $ACu_3Ti_3FeO_{12}$ Phases. *Journal of Solid State Chemistry*, 151:323–325, 2000. URL `http://www.ingentaconnect.com/content/ap/sc/2000/00000151/00000002/art08703`.

[5] Yuanhua Lin, Lei Jiang, Rongjuan Zhao, and Ce-Wen Nan. High-permittivity core/shell stuctured NiO-based ceramics and their dielectric response mechanism. *Physical Review B*, 72:014103, 2005.

[6] Sophie Guillemet-Fritsch, Zarel Valdez-Nava, Christophe Tenailleau, Thierry Lebey, Bernard Durand, and Jean-Yves Chane-Ching. Colossal Permittivity in Ultrafine Grain Size $BaTiO_{3-x}$ and $Ba_{0.95}La_{0.05}TiO_{3-x}$ Materials. *Adv. Mater.*, 20:551–555, 2008.

[7] S. Krohns, P. Lunkenheimer, Ch. Kant, A. V. Pronin, H. B. Brom, A. A. Nugroho, M. Diantoro, and A. Loidl. Colossal dielectric constant up to GHz at room temperature. *Applied Physics Letters*, 91:122903, 2009. doi: 10.1063/1.3105993. URL `http://arxiv.org/abs/0811.1556v2`.

[8] P. Ren, Z. Yang, W. G. Zhu, C. H. A. Huan, and L. Wang. Origin of the colossal dielectric permittivity and magnetocapacitance in $LuFe_2O_4$. *Journal of Applied Physics*, 109:074109, 2011.

[9] David J. Griffiths. *Introduction to Electrodynamics*. Pearson Addison-Wesley, Upper Saddle River, New Jersey, USA, 1999.

[10] Patrick Fiorenza, Raffaella Lo Nigro, and Vito Raineri. Colossal Permittivity in Advanced Functional Heterogeneous Materials: The Relevance of the Local Measurements at Submicron Scale. In Bharat Bhushan, editor, *Scanning Probe Microscopy in Nanoscience and Nanotechnology*, NanoScience and Technology, pages 613–646. Springer Berlin Heidelberg, 2010. ISBN 978-3-642-03534-0.

[11] Mingrong Shen, Shuibing Ge, and Wenwu Cao. Dielectric enhancement and Maxwell-Wagner effects in polycrystalline ferroelectric multilayered thin films. *Journal of Physics D: Applied Physics*, 34:2935–2938, 2001.

[12] Anonymous. An Overview of Ultracapacitor Technology, 2014. URL `http://www.maxwell.com/ultracapacitors/`. [Online; accessed 08-April-2014].

[13] D. A. Crandles, S. M. M. Yee, M. Savinov, D. D. Nuzhnyy, J. Petzelt, S. Kamba, and J. Prokeš. Electrode effects in dielectric spectroscopy measurements on (Nb+In) co-doped TiO_2. *Journal of Applied Physics*, 119:154105, 2016. doi: 10.1063/1.4947185.

[14] Zhigang Gai, Zhenxiang Cheng, Xiaolin Wang, Lanling Zhao, Na Yin, Roza Abah, Minglei Zhao, Fang Hong, Zheyin Yu, and Shixue Dou. A colossal dielectric constant of an amorphous TiO_2:(Nb, In) film with low loss fabrication at room temperature. *Journal of Materials Chemistry C*, 2:6790, June 2014. doi: 10.1039/c4tc00500g.

[15] Christopher C. Homes and Thomas Vogt. Colossal permittivity materials: Doping for superior dielectrics. *Nature Materials*, 12:782–783, 2013. doi: doi:10.1038/nmat3744. Published online 22 August 2013.

[16] Jinglei Li, Fei Li, Yongyong Zhuang, Li Jin, Linghang Wang, Xiaoyong Wei, Zhuo Xu, and Shujun Zhang. Microstructure and dielectric properties of (Nb + In) co-doped rutile TiO_2 ceramics. *Journal of Applied Physics*, 116:074105, 2014. doi: 10.1063/1.4893316.

[17] Jinglei Li, Fei Li, Chao Li, Guang Yang, Zhuo Xu, and Shujun Zhang. Evidences of grain boundary capacitance effect on the colossal dielectric permittivity in (Nb+In) co-doped TiO_2 ceramics. *Scientific Reports*, 5, February 2015. doi: 10.1038/srep08295.

[18] F. Matteucci, G. Cruciani, M. Dondi, and M. Raimondo. The role of counterions (Mo, Nb, Sb, W) in Cr-, Mn-, Ni- and V-doped rutile ceramic pigments Part 1. Crystal structure and phase transformations. *Ceramics International*, 32:385–392, 2006. doi: 10.1016/j.ceramint.2005.03.014.

[19] L. Miao, Y. Xin, H. Zhu, H. Xu, S. Luo, D. Talbayev, T. N. Stanislavchuk, A. A. Sirenko, and Z. Mao. Colossal permittivity induced by lattice mirror reflection symmetry breaking in $Ba_7Ir_3O_{13+x}$ (0 <= x <= 1.5) epitaxial thin films. In *APS Meeting Abstracts*, page 41012, March 2014.

[20] Osamu Tonomura, Tomoko Sekiguchi, Naomi Inada, Tomoyuki Hamada, Hiroshi Miki, and Kazuyoshi Torii. Band Engineering of Ru/Rutile-TiO_2/Ru Capacitors by Doping Cobalt to Suppress Leakage Current. *J. Electrochem. Soc.*, 159(1):G1–G5, 2012. doi: doi:10.1149/2.040201jes.

[21] S. S. Batsanov, V. I. Galko, and K. V. Papugin. Dielectric Permittivity and Electrical Conductivity of Polycrystalline Materials. *Inorganic Materials*, 46(12):1365–1368, 2010.

[22] Chafe Cheballah, Zarel Valdez-Nava, Lionel Laudebat, Thierry Lebey, Pierre Bidan, Sombel Diaham, and Sophie Guillemet-Fritsch. Dielectric Properties of Colossal Permittivity Materials: An Update. *Journal of Energy and Power Engineering*, 7: 726–732, 2013.

[23] Hyuksu Han, Dipankar Ghosh, Jacob L. Jones, and Juan C. Nino. Colossal Permittivity in Microwave-Sintered Barium Titanate and Effect of Annealing on Dielectric Properties. *Journal of the American Ceramic Society*, 96(2):485–490, 02 2013.

[24] Hyuksu Han, Christophe Voisin, Sophie Guillemet-Fritsch, Pascal Dufour, Christophe Tenailleau, Christopher Turner, and Juan C. Nino. Origin of colossal permittivity in $BaTiO_3$ via broadband dielectric spectroscopy. *Journal of Applied Physics*, 113(2):024102, 2013.

[25] Hyuksu Han, Calvin Davis, III, and Juan C. Nino. Variable Range Hopping Conduction in $BaTiO_3$ Ceramics Exhibiting Colossal Permittivity. *Journal of Physical Chemistry C*, 118:9137–9142, 2014. doi: 10.1021/jp502314r.

[26] Thierry Lebey, Sophie Guillemet, Vincent Bley, Madona Boulos, and Bernard Durand. Origin of the Colossal Permittivity and Possible Application of CCT Ceramics. In *Electronic Components and Technology Conference*. IEEE, 2005.

[27] Wei Li and Robert W. Schwartz. Maxwell-Wagner relaxations and their contributions to the high permittivity of calcium copper titanate ceramics. *Physical Review B*, 75:012104, 2007.

[28] R. F. Mamin, T. Egami, Z. Marton, and S. A. Migachev. Giant Dielectric Permittivity and Colossal Magnetocapacitance Effect in Complex Manganites with High Conductivity. *Ferroelectrics*, 348:7–12, 2007.

[29] Derek C. Sinclair, Timothy B. Adams, Finlay D. Morrison, and Anthony R. West. $CaCu_3Ti_4O_{12}$: One-step internal barrier layer capacitor. *Applied Physics Letters*, 80 (12):2153–2155, March 2002. doi: 10.1063/1.1463211.

[30] C. C. Homes, T. Vogt, S. M. Shapiro, S. Wakimoto, and A. P. Ramirez. Optical Response of High-Dielectric-Constant Perovskite-Related Oxide. *Science*, 293:673, July 2001. doi: 10.1126/science.1061655.

[31] Lei Zhang and Zhong-Jia Tang. Polaron relaxation and variable-range-hopping conductivity in the giant-dielectric-constant material $CaCu_3Ti_4O_{12}$. *Physical Review B*, 70:174306, 2004.

[32] Yun Liu, Ray L. Withers, and Xiao Yong Wei. Structurally frustrated relaxor ferroelectric behavior in $CaCu_3Ti_4O_{12}$. *Physical Review B*, 72:134104, 2005. doi: 10.1103/PhysRevB.72.134104.

[33] C. C. Wang and L. W. Zhang. Oxygen-vacancy-related dielectric anomaly in $CaCu_3Ti_4O_{12}$: Post-sintering annealing studies. *Physical Review B*, 74:024106, 2006. doi: 10.1103/PhysRevB.74.024106.

[34] Ch. Kant, T. Rudolf, F. Mayr, S. Krohns, P. Lunkenheimer, S. G. Ebbinghaus, and A. Loidl. Broadband dielectric response of $CaCu_3Ti_4O_{12}$: From dc to the electronic transition regime. *Physical Review B*, 77:045131, 2008. doi: 10.1103/PhysRevB.77.045131.

[35] Sabar D. Hutagalung, Mohd Ikhwan M. Ibrahim, and Zainal A. Ahmad. The role of tin oxide addition on the properties of microwave treated $CaCu_3Ti_4O_{12}$. *Materials Chemistry and Physics*, 112(1):83–87, November 2008. URL `http://www.sciencedirect.com/science/article/pii/S025405840800285X`.

[36] S. Krohns, P. Lunkenheimer, S. G. Ebbinghaus, and A. Loidl. Colossal dielectric constants in single-crystalline and ceramic $CaCu_3Ti_4O_{12}$ investigated by broadband dielectric spectroscopy. *J. Appl. Phys.*, 103:084107, 2008. doi: 10.1063/1.2902374. URL `http://arxiv.org/abs/0710.1610`.

[37] Guochu Deng and Paul Muralt. Annealing effects on electrical properties and defects of $CaCu_3Ti_4O_{12}$ thin films deposited by pulsed laser deposition. *Physical Review B*, 81:224111, 2010. doi: 10.1103/PhysRevB.81.224111.

[38] Fengchao Luo, Jinliang He, and Jun Hu. Electric and Dielectric Behaviors of Y-Doped Calcium Copper Titanate. *Journal of the Amercan Ceramic Society*, 93(10): 3043–3045, 2010. doi: 10.1111/j.1551-2916.2010.04022.x.

[39] J. Sebald, S. Krohns, P. Lunkenheimer, S.G. Ebbinghaus, S. Riegg, A. Reller, and A. Loidl. Colossal dielectric constants: A common phenomenon in $CaCu_3Ti_4O_{12}$ related materials. *Solid State Communications*, 150:857–860, 2010.

[40] F. Amaral, L.C. Costa, M.A. Valente, A.J.S. Fernandes, N. Franco, E. Alves, and F.M. Costa. Colossal dielectric constant of poly- and single-crystalline $CaCu_3Ti_4O_{12}$ fibres grown by the laser floating zone technique. *Acta Materialia*, 59:102–111, 2011.

[41] Jianjun Liu, Chun-Gang Duan, Wei-Guo Yin, W. N. Mei, R. W. Smith, and John R. Hardy. Large Dielectric Constant and Maxwell-Wagner Relaxation in $Bi_{2/3}Cu_3Ti_4O_{12}$. *Physical Review B*, 70:144106, 2004. doi: 10.1103/PhysRevB.70.144106.

[42] A. Wall and G. D. Price. A computer simulation of the structure and elastic properties of $MgSiO_3$ perovskite. *Mineralogical Magazine*, 50:693–707, December 1986.

[43] I. M. Reaney, J. Petzelt, V. V. Voitsekhovskii, F. Chu, and N. Setter. B-site order and infrared reflectivity in A(B'B")O3 complex perovskite ceramics. *Journal of Applied Physics*, 76:2086, 1994. doi: 10.1063/1.357618.

[44] Mehmet A. Akbas and Peter K. Davies. Structure and Dielectric Properties of the $Ba(Mg_{1/3}Nb_{2/3})O_3$-$La(Mg_{2/3}Nb_{1/3})O_3$ System. *Journal of the American Ceramic Society*, 81(8):2205–2208, 1998.

[45] Liang Chai and Peter K. Davies. Formation and Structural Characterization of 1:1 Ordered Perovskites in the $Ba(Zn_{1/3}Ta_{2/3})O_3$-$BaZrO_3$ System. *Journal of the American Ceramic Society*, 80(12):3193–3198, 1997.

[46] T. Thonhauser and K. M. Rabe. Fcc breathing instability in $BaBiO_3$ from first principles. *Physical Review B*, 73:212106, June 2006. doi: 10.1103/PhysRevB.73.212106.

[47] Hui Wu and Peter K. Davies. Influence of Non-Stoichiometry on the Structure and Properties of $Ba(Zn_{1/3}Nb_{2/3})O_3$ Microwave Dielectrics: II. Compositional Variations in Pure BZN. *Journal of the American Ceramic Society*, 89(7):2250–2263, 2006. doi: 10.1111/j.1551-2916.2006.01008.x.

[48] Dmytro Grebennikov and Peter Mascher. Structural properties of near-stoichiometric composition of $Ba(B'_{1/3}B''_{2/3})\ O_3$ (B'=Mg, Co, or Zn and B"=Nb or Ta) perovskites. *Journal of Materials Research*, 26(9):1116–1125, May 2011. doi: 10.1557/jmr.2011.58.

[49] Mohammad A Islam, James M Rondinelli, and Jonathan E Spanier. Normal mode determination of perovskite crystal structures with octahedral rotations: theory and applications. *Journal of Physics: Condensed Matter*, 25(17):175902, 2013. URL `http://stacks.iop.org/0953-8984/25/i=17/a=175902`.

[50] Perovskite (structure). Perovskite (structure) — Wikipedia, the free encyclopedia, 2015. URL `https://en.wikipedia.org/wiki/Perovskite_(structure)?oldid=678313806`. [Online; accessed 2015-September-11].

[51] Maria Teresa Buscaglia, Massimo Viviani, Vincenzo Buscaglia, Liliana Mitoseriu, Andrea Testino, Paolo Nanni, Zhe Zhao, Mats Nygren, Catalin Harnagea, Daniele Piazza, and Carmen Galassi. High dielectric constant and frozen macroscopic polarization in dense nanocrystalline $BaTiO_3$ ceramics. *Phys. Rev. B*, 73:064114, Feb 2006. doi: 10.1103/PhysRevB.73.064114. URL `http://link.aps.org/doi/10.1103/PhysRevB.73.064114`.

[52] Yong Jun Wu, Shao Hua Su, Ji Peng Cheng, and Xiang Ming Chen. Spark Plasma Sintering of Barium Zirconate Titanate/Carbon Nanotube Composites with Colossal

Dielectric Constant and Low Dielectric Loss. *Journal of the American Ceramic Society*, 94(3):663–665, March 2011. doi: 10.1111/j.1551-2916.2010.04361.x. URL `http://dx.doi.org/10.1111/j.1551-2916.2010.04361.x`. Article first published online: 15 FEB 2011.

[53] Th. Hölbling, N. Söylemezoğlu, and R. Waser. A Mathematical-Physical Model for the Charge Transport in p-Type SrTiO3 Ceramics Under dc Load: Maxwell-Wagner Relaxation. *Journal of Electroceramics*, 9(2):87–100, November 2002.

[54] Cheng Liu, Peng Liu, Jian-ping Zhou, Ying He, Li-na Su, Lei Cao, and Huai-wu Zhang. Colossal dielectric constant and relaxation behaviors in Pr:$SrTiO_3$ ceramics. *Journal of Applied Physics*, 107:094108, 2010.

[55] Y. Q. Lin, Y. J. Wu, S. P. Gu, and X. M. Chen. Contribution of Electron Hopping on Colossal Dielectric Response of Bi-Substituted $LaMnO_3$ Ceramics. *Ferroelectrics*, 388:133–139, 2009.

[56] Sudipta Sarkar, Pradip Kumar Jana, and B. K. Chaudhuri. Colossal internal barrier layer capacitance effect in polycrystalline copper (II) oxide. *Applied Physics Letters*, 92:022905, 2008.

[57] Sten Andersson, Bengt Collén, Ulf Kuylenstierna, and Arne Magnéli. Phase Analysis Studies on the Titanium-Oxygen System. *Acta Chemica Scandinavica*, 11:1641–1652, 1957.

[58] L N. Shen, O. W. Johnson, W. D. Ohlsen, and John W. DeFord. Reinterpretation of the "Ti^{3+} interstitial" electron-spin-resonance spectrum in rutile. *Physical Review B*, 10(5):1823–1825, September 1974.

[59] Ph. Odier, J. F. Baumard, D. Panis, and A. M. Anthony. Thermal Emission, Electrical Conductivity, and Hall Effect for Defects Study at High Temperature (T>=1250°K) in Refractory Oxides (Y_2O_3,TiO_2). *Journal of Solid State Chemistry*, 12:324–328, 1975.

[60] Michael A. Henderson. Evidence for bicarbonate formation on vacuum annealed TiO_2(110) resulting from a precursor-mediated interaction between CO_2 and H_2O. *Surface Science*, 400:203–219, 1998.

[61] M.K. Nowotny, P. Bogdanoff, T. Dittrich, S. Fiechter, A. Fujishima, and H. Tributsch. Observations of p-type semiconductivity in titanium dioxide at room temper-

ature. *Materials Letters*, 64(8):928–930, April 2010. doi: 10.1016/j.matlet.2010.01.061.

[62] Xiao Qiang Wang, Jian Min Wang, Jing Guo, and Yue Liu Li Ming Ya Li. Preparation of New Structural TiO_2 Nanotube Arrays and Study of Photoelectric Properties. In Hu et al. [110], pages 212–215. ISBN 978-3-03785-567-6. doi: 10.4028/www.scientific.net/AMR.624.212.

[63] Aleksandra Wypych, Izabela Bobowska, Milena Tracz, Agnieszka Opasinska, Slawomir Kadlubowski, Alicja Krzywania-Kaliszewska, Jaroslaw Grobelny, and Piotr Wojciechowski. Dielectric Properties and Characterisation of Titanium Dioxide Obtained by Different Chemistry Methods. *Journal of Nanomaterials*, 2014, 2014. doi: 10.1155/2014/124814. Article ID 124814.

[64] P. F. Chester. Cross Doping Agents for Rutile Masers. *Journal of Applied Physics*, 32(5):866, May 1961. doi: 10.1063/1.1736120.

[65] N. G. Eror. Self-Compensation in Niobium-Doped TiO_2. *Journal of Solid State Chemistry*, 38:281–287, 1981.

[66] Jean-Francis Marucco, Bertrand Poumellec, Jacques Gautron, and Philippe Lemasson. Thermodynamic Properties of Titanium Dioxide, Niobium Dioxide and Their Solid Solutions at High Temperature. *Journal of Physics and Chemistry of Solids*, 46(6):709–717, 1985.

[67] B. Poumellec, J. F. Marucco, and F. Lagnel. Electron Transport in $Ti_{1-x}Nb_xO_2$ Solid Solutions with x<4%. *Journal of Physics and Chemistry of Solids*, 41(4):381–385, 1986.

[68] S. X. Zhang, D. C. Kundaliya, W. Yu, S. Dhar, S. Y. Young, L. G. Salamanca-Riba, S. B. Ogale, R. D. Vispute, and T. Venkatesan. Niobium doped TiO_2: Intrinsic transparent metallic anatase versus highly resistive rutile phase. *Journal of Applied Physics*, 102:013701, 2007. doi: 10.1063/1.2750407.

[69] Enjun Wang, Wensheng Yang, and Yaan Cao. Unique Surface Chemical Species on Indium Doped TiO_2 and Their Effect on the Visible Light Photocatalytic Activity. *Journal of Physical Chemistry C*, 113:20912–20917, 2009. doi: 10.1021/jp9041793.

[70] Armand J. Atanacio, Tadeusz Bak, and Janusz Nowotny. Niobium Segregation in Niobium-Doped Titanium Dioxide (Rutile). *Journal of Physical Chemistry C*, 118: 11174–11185, 2014. doi: 10.1021/jp4110536.

[71] S.K. Mukherjee, H.W. Becker, A.P. Cadiz Bedini, A. Nebatti, C. Notthoff, D. Rogalla, S. Schipporeit, A. Soleimani-Esfahani, and D. Mergel. Structural and electrical properties of Nb-doped TiO_2 films sputtered with plasma emission control. *Thin Solid Films*, 568:94–101, October 2014. doi: 10.1016/j.tsf.2014.08.011.

[72] D. K. Philp and L. A. Bursill. Phase Analysis Studies of Titanium-Chromium Oxides Derived from Rutile by Crystallographic Shear. *Journal of Solid State Chemistry*, 10:357–370, 1974.

[73] S. Zhao, H. L. Wan, and S. Asuha. Preparation and Properties of Eu^{3+}-Doped TiO_2 Nanowires. In Hu et al. [110], pages 67–71. ISBN 978-3-03785-567-6.

[74] Kirit S. Siddhapara and D.V. Shah. Synthesis, Structural, Optical, and Magnetic Properties of Fe Doped TiO_2 along with Different Concentration. In Prafulla K. Jha and Arun Pratap, editors, *Condensed Matter and Materials Physics*, pages 118–126. Trans Tech Publications, 2013. ISBN 978-3-03785-625-3.

[75] Ferroelectricity. Ferroelectricity — Wikipedia, the free encyclopedia, 2013. URL `http://en.wikipedia.org/w/index.php?oldid=551438779`. [Online; accessed 2013-May-11].

[76] Charles Kittel. *Introduction to solid state physics*. John Wiley and Sons, Inc., New York, NY, USA, 8 edition, 2005. ISBN 047141526X.

[77] P. Lunkenheimer, V. Bobnar, A. V. Pronin, A. I. Ritus, A. A. Volkov, and A. Loidl. Origin of apparent colossal dielectric constants. *Physical Review B*, 66(5):052105, August 2002. doi: 10.1103/PhysRevB.66.052105. URL `http://link.aps.org/doi/10.1103/PhysRevB.66.052105`.

[78] P. Lunkenheimer, S. Krohns, S. Riegg, S.G. Ebbinghaus, A. Reller, and A. Loidl. Colossal dielectric constants in transition-metal oxides. *The European Physical Journal Special Topics*, 180:61–89, 2010. doi: 10.1140/epjst/e2010-01212-5.

[79] C. C. Wang and L. W. Zhang. Polaron relaxation related to localized charge carriers in $CaCu_3Ti_4O_{12}$. *Applied Physics Letters*, 90:142905, 2007. doi: 10.1063/1.2719608.

[80] Charge density wave. Charge density wave — Wikipedia, the free encyclopedia, 2015. URL `https://en.wikipedia.org/wiki/Charge_density_wave?oldid=670548471`. [Online; accessed 2015-October-02].

[81] Ravindra Pankaj and Sudhakar Yarlagadda. Study of cooperative breathing-mode in molecular chains. *Physical Review B*, 86:035453, 2012. doi: 10.1103/PhysRevB.86.035453.

[82] Xuetao Zhu, Yanwei Cao, Jiandi Zhang, E. W. Plummer, and Jiandong Guo. Classification of charge density waves based on their nature. *Proceedings of the National Academy of Sciences of the United States of America*, 112(8):2367–2371, February 2015. doi: 10.1073/pnas.1424791112.

[83] N.P. Ong. Charge Density Wave [Online Notes], 2012. URL `http://www.princeton.edu/~npo/SurveyTopics/CDW/ChargeDensityWave.html`. [Online; accessed 2015-October].

[84] David R. Rosseinsky, Jamal A. Stephan, and James S. Tonge. Site-transfer Electronic Conductivity: The Hopping or Polaron (Direct-current) Mechanism from Dielectric Relaxation Studies on Intervalence Mixtures and Charge-transfer Adducts. *Journal of the Chemical Society, Faraday Transactions 1*, 77:1719–1727, 1981. doi: 10.1039/F19817701719. URL `http://dx.doi.org/10.1039/F19817701719`.

[85] Harald F. Hess, Keith DeConde, T. F. Rosenbaum, and G. A. Thomas. Giant dielectric constants at the approach to the insulator-metal transition. *Physical Review B*, 25(8):5578–5580, April 1982.

[86] M. S. Dresselhaus. Applications of group theory to the physics of solids, 2002. URL `web.mit.edu/course/6/6.734j/www/group-full02.pdf`. [Online; accessed 2016-March].

[87] Francois Gervais and Bernard Piriou. Temperature dependence of transverse- and longitudinal-optic modes in TiO_2 (rutile). *Phys. Rev. B*, 10:1642–1654, Aug 1974. doi: 10.1103/PhysRevB.10.1642. URL `http://link.aps.org/doi/10.1103/PhysRevB.10.1642`.

[88] David M. Bishop. *Group Theory and Chemistry*. Dover, 1993. ISBN 0-486-67355-3.

[89] Naoki Matsumoto, Tadasu Hosokura, Keisuke Kageyama, Hiroshi Takagi, Yukio Sakabe, and Masanori Hangyo. Analysis of Dielectric Response of TiO_2 in Terahertz Frequency Region by General Harmonic Oscillator Model. *Japanese Journal of Applied Physics*, 47(9S):7725, 2008. URL `http://stacks.iop.org/1347-4065/47/i=9S/a=7725`.

[90] David B. Tanner. Optical effects in solids, 2016. URL `http://www.phys.ufl.edu/~tanner/notes.pdf`. [Online; accessed 2016-January].

[91] C.C. Homes, M. Reedyk, D.A. Crandles, and T. Timusk. Technique for measuring the reflectance of irregular, submillimeter-sized samples. *Applied Optics*, 32, 1993.

[92] J. G. Traylor, H. G. Smith, R. M. Nicklow, and M. K. Wilkinson. Lattice Dynamics of Rutile. *Physical Review B*, 3(10):3457–3471, 1971.

[93] Björn Wehinger, Alexeï Bosak, and Paweł T. Jochym. Soft phonon modes in rutile TiO_2. *Physical Review B*, 93:014303, 2016. doi: 10.1103/PhysRevB.93.014303.

[94] Manuel Cardona and Gunther Harbeke. Optical Properties and Band Structure of Wurtzite-Type Crystals and Rutile. *Physical Review*, 137(5A), March 1965.

[95] D. B. Tanner. Use of x-ray scattering functions in Kramers-Kronig analysis of reflectance. *Physical Review B*, 91:035123, 2015. doi: 10.1103/PhysRevB.91.035123.

[96] B.L. Henke, E.M. Gullikson, and J.C. Davis. X-ray interactions: Photoabsorption, scattering, transmission, and reflection at e = 50-30,000 ev, z = 1-92. *Atomic Data and Nuclear Data Tables*, 54(2):181–342, 1993. ISSN 0092-640X. doi: http://dx.doi.org/10.1006/adnd.1993.1013. URL `http://www.sciencedirect.com/science/article/pii/S0092640X83710132`.

[97] Dr. C.C. Homes. personal communication, April 2017.

[98] S. P. S. Porto, P. A. Fleury, and T. C. Damen. Raman Spectra of TiO_2, MgF_2, ZnF_2, FeF_2, and MnF_2. *Physical Review*, 154(2):522–526, February 1967.

[99] P A Fleury. The effects of soft modes on the structure and properties of materials. *Annual Review of Materials Science*, 6(1):157–180, 1976. doi: 10.1146/annurev.ms.06.080176.001105. URL `http://dx.doi.org/10.1146/annurev.ms.06.080176.001105`.

[100] N. Nakanishi, A. Nagasawa, and Y. Murakami. LATTICE STABILITY AND SOFT MODES. *Journal de Physique Colloques*, 43(Colloque C4 - number 12):C4–35–C4–55, December 1982. doi: 10.1051/jphyscol:1982403.

[101] W. Cochran. Crystal stability and the theory of ferroelectricity. *Advances in Physics*, 9:387–423, October 1960. doi: 10.1080/00018736000101229.

[102] Cheng Cen, Maitri P. Warusawithana, Darrell G. Schlom, and Jeremy Levy. Coherent phonon generation and detection in ultrathin $SrTiO_3$ grown directly on silicon. *Annalen der Physik*, 524, 2012.

[103] V. Goian, S. Kamba, C. Kadlec, D. Nuzhnyy, P. Kužel, J. Agostinho Moreira, A. Almeida, and P.B. Tavares. THz and infrared studies of multiferroic hexagonal $Y_{1-x}Eu_xMnO_3$ (x=0 - 0.2) ceramics. *Phase Transitions*, 83:931–941, 2010. doi: 10.1080/01411594.2010.509603.

[104] D. Nuzhnyy, J. Petzelt, S. Kamba, P. Kužel, C. Kadlec, V. Bovtun, M. Kempa, J. Schubert, C. M. Brooks, and D. G. Schlom. Soft mode behavior in $SrTiO_3$/$DyScO_3$ thin films: Evidence of ferroelectric and antiferrodistortive phase transitions. *Applied Physics Letters*, 95:232902, 2009. doi: 10.1063/1.3271179.

[105] G. Shirane, J. D. Axe, J. Harada, and J. P. Remeika. Soft Ferroelectric Modes in Lead Titanate. *Phys. Rev. B*, 2:155–159, July 1970. doi: 10.1103/PhysRevB.2.155. URL `http://link.aps.org/doi/10.1103/PhysRevB.2.155`.

[106] A.A. Sirenko, C. Bernhard, A. Golnik, Anna M. Clark, Jianhua Hao, Weidong Si, and X. X. Xi. Soft-mode hardening in $SrTiO_3$ thin films. *Nature*, 404:373–376, March 2000. doi: 10.1038/35006023.

[107] V. Železný, Eric Cockayne, J. Petzelt., M. F. Limonov, D. E. Usvyat, V. V. Lemanov, and A. A. Volkov. Temperature dependence of infrared-active phonons in $CaTiO_3$: A combined spectroscopic and first-principles study. *Phys. Rev. B*, 66:224303, Dec 2002. doi: 10.1103/PhysRevB.66.224303. URL `http://link.aps.org/doi/10.1103/PhysRevB.66.224303`.

[108] D. Nuzhnyy, J. Petzelt, I. Rychetsky, and G. Trefalt. Effective dielectric function of porous $Pb(Mg_{1/3}Nb_{2/3})O_3$ ceramics. *Physical Review B*, 89:214307, 2014. doi: 10.1103/PhysRevB.89.214307.

[109] Tarik Zakri, Jean-Paul Laurent, and Michel Vauclin. Theoretical evidence for "Lichtenecker's mixture formulae" based on the effective medium theory. *Journal of Physics D: Applied Physics*, 31(13):1589–1594, July 1998. doi: 10.1088/0022-3727/31/13/013.

[110] Jin Hu, Nanchun Chen, and Cheng Zhang, editors. *2012 Workshop on Synthesis, Characterization and Applications of Inorganic Powders*, 2013. Trans Tech Publications. ISBN 978-3-03785-567-6.

Appendix A

Phonons

Lattice vibrations contain energy. This vibrational energy is quantized [76]. In an analogy with the energy quanta of electromagnetic field vibrations, which are called photons, the energy quanta of lattice vibrations are called phonons. The vibrations lead to waves in the lattice of the solid (mechanical elastic waves), which result in displacements of the atoms from their equilibrium position. Transverse waves are those in which the atomic displacements are orthogonal to the direction of the propagation of the wave (Fig. A.0.1). Longitudinal waves are those in which the atomic displacements are parallel to the direction of the propagation of the wave (fig. A.0.2). In three dimensional solids there are two transverse vibrational modes.

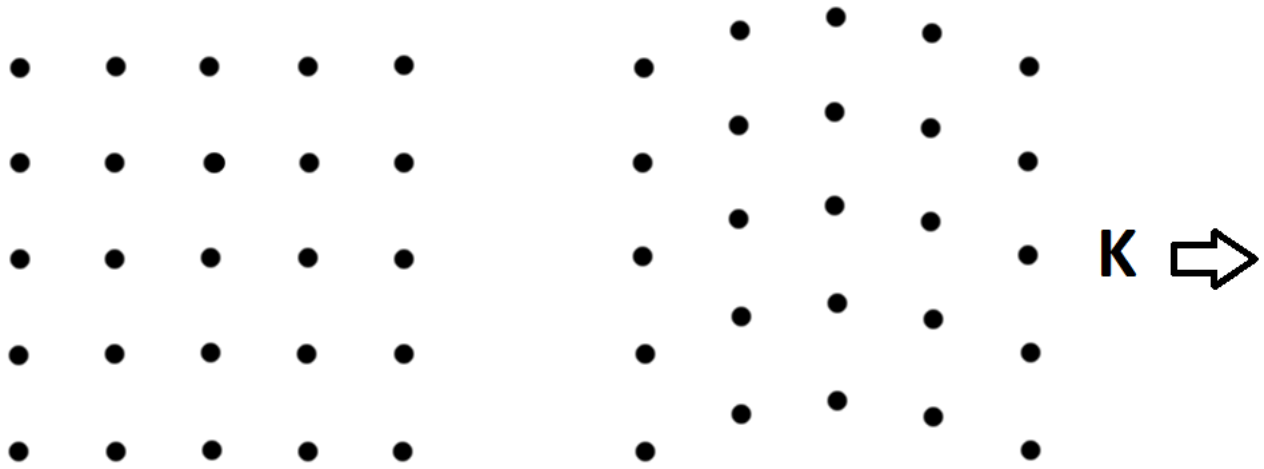

Figure A.0.1: Transverse Wave
The 5X5 grid on the left shows the equilibrium position of the atoms in the lattice. K is the wave vector and shows the direction of the propagation of the phonon.

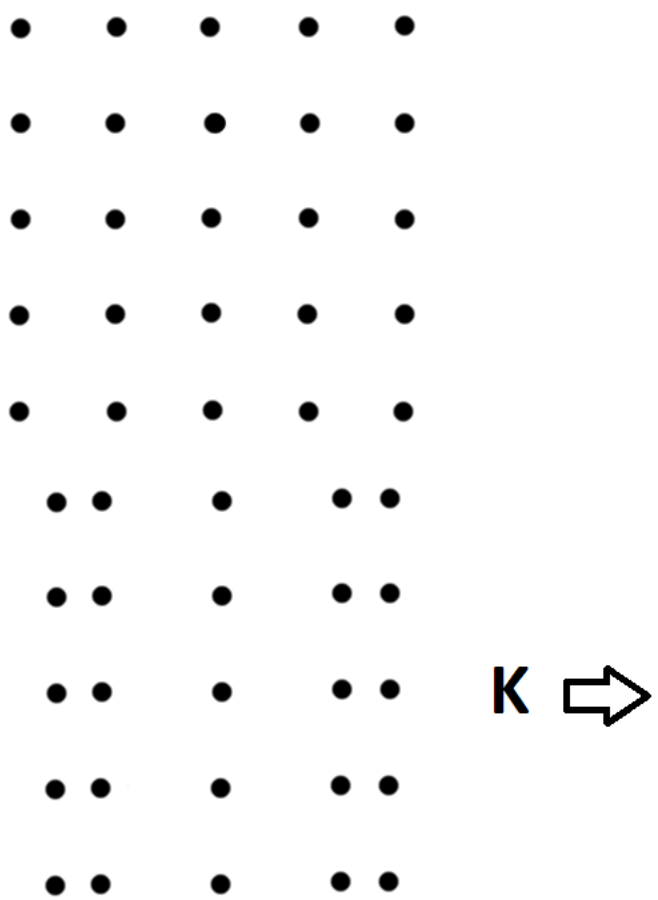

Figure A.0.2: Longitudinal Wave
The 5X5 grid on the top shows the equilibrium position of the atoms in the lattice. K is the wave vector and shows the direction of the propagation of the phonon.

The transverse waves can be stimulated by the electric field of visible light in which case the mode is called a transverse optical mode. Transverse waves can also be stimulated at lower frequencies in which case the mode is called a transverse acoustical mode[76]. Similarly, we have longitudinal optical and acoustical modes.

Appendix B

Group Theory Predictions

The symmetry operations on an octahedron (see [86]):

(a) rotations about the axes perpendicular to each of the 8 triangular faces - 8 axes each one consisting of $\frac{2\pi}{3}$ rotations; named C_3

(b) rotations about the axes passing through the six vertices (and through the center) of the octahedron - 6 axes each one consisting of $\frac{\pi}{2}$ rotations; named C_4

(c) rotations about the axes passing through the six vertices (and through the center) of the octahedron - 6 axes each one consisting of π rotations. A rotation of π does not give the same configuration as a rotation of $\frac{\pi}{2}$. Therefore, this set of rotations is different from the set in (b). However, a rotation of π about a vertex V will give the same configuration as a rotation of π about the opposite vertex. Therefore, instead of six C_2 rotations there are three. A rotation C_2 equals two succesive C_4 rotations, i.e. $(C_4)^2$.

(d) rotations about axes passing through the midpoints of the edges - 3 axes each one consisting of π rotations; also named C_2

(e) an inversion through the center of the octahedron; named i (not the same as the the imaginary number $\sqrt{-1}$)

(f) "do nothing" or leave the octahedron alone; named e (or E)

These symmetry operations form a group, Group O_h. Note that the operations and not the vertices of the octahedron are the elements of the group O.

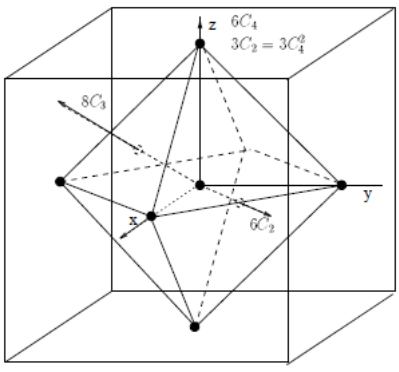

Figure B.0.1: From [86]

Inversion symmetry operations that preserve the same sign are called even and are labelled with a subscript g (German "gerade" meaning even). Inversion operations that change sign are called odd and are labelled with a subscript u (German "ungerade" meaning not-even or odd).

Group elements (the rotation and inversion operations) can be represented by square matrices and the operations on the octahedron are calculated by the usual matrix multiplication. This set of matrices is called a representation. The set of matrices (the representation) representing the group elements is not unique. For instance, applying the same matrix similarity transform on all of the matrices will produce another set of matrices which is also a representation of the group. A similarity transformation can reduce the matrix to a simpler one consisting of a diagonal composed of smaller square matrices - block diagonalize all the matrices. These smaller blocks can be used as matrices in of themselves as a representation. If it is impossible to block diagonalize all of the matrices in a representation using the same similarity transformation, then the representation is called irreducible.

From linear algebra it is known that the trace of a matrix is invariant under similarity transformations. This means that different but similar representations have the same set of traces. The trace of a matrix in a representation is called the character of the matrix. The irreducible representations can be characterized by the set of traces of the matrices in the representation. In this way, the irreducible representations and their relationships among the symmetry operations can be characterized by a table of traces called a character table. It is not necessary to liast an actual matrix representing a specific operation. It is important to note that there are several irreducible representations for a group. For Group O_h there are 10 distinct irreducible representations. Character tables are widely published so it is not necessary to calculate them.

The character tables are very important becuase it is possible to calculate some properties of the symmetry group by using simple arithmetic on the characters in the character table and not have to do any matrix operations.

Infrared active modes involve excitations of dipoles; that is, displacements of atoms and electrons. Displacement is a vector and vectors change sign under inversion. That means symmetry operations on the Schrodinger equation involving dipole displacements are odd or ungerade. Therefore, vibrational modes that are ungerade can be infrared-active [86].

The Raman effect involves the polarizability tensor which is a second rank, symmetric tensor. In this kind of tensor the components are quadratics which do not change sign under inversion. The symmetry operations on the Schrodinger equation are even or gerade. Therefore, vibrational modes that are gerade can be Raman active [86].

Note that a vibrational mode cannot be both gerade and ungerade simultaneously. This

means an infrared active mode cannot be Raman active and a Raman active mode cannot be infrared active. This is what is meant when it is said that infrared and Raman spectroscopy are complementary techniques.

The application of group theory shows that the infrared-active modes of vibration of the rutile crystal are A_{2u} and E_u. Infrared radiation excites dipole moments. Dipoles involve the spatial displacement of charge where displacement involves the coordinate functions (x, y, z). The unit cell of the rutile form of TiO_2 is a body-centered tetragonal structure. The symmetry of this structure is the D_{4h} point group[86]. In this symmetry group the basis functions (x, y, z) correspond to the irreducible representations A_{2u} and E_u. This means the excitation of dipole moments occurs for vibrational modes that show A_{2u} and E_u symmetry. Therefore, infrared radiation excites the vibrational modes A_{2u} and E_u in rutile, or the A_{2u} and E_u modes are infrared active. For a detailed explanation of the application of group theory to solids see [86, 88].